Master's Thesis

SOLID-STATE SYNTHESIS OF LOW DIMENSIONAL LEAD-FREE Mn-BASED FLUORESCENT ORGANIC-INORGANIC HYBRID COMPOUNDS

Shynggys Zhumagali

Department of Chemistry

Graduate School of UNIST

2019

SOLID-STATE SYNTHESIS OF LOW DIMENSIONAL LEAD-FREE Mn-BASED FLUORESCENT ORGANIC-INORGANIC HYBRID COMPOUNDS

Shynggys Zhumagali

Department of Chemistry

Graduate School of UNIST

Solid-State Synthesis of Low Dimensional Lead-Free Mn-Based Fluorescent Organic-Inorganic Hybrid Compounds

A thesis
submitted to the Graduate School of UNIST
in partial fulfillment of the
requirements for the degree of
Master of Science

Shynggys Zhumagali

06. 27. 2019
Approved by

Advisor
Kwang S. Kim

Solid-State Synthesis of Low Dimensional Lead-Free Mn-Based Fluorescent Organic-Inorganic Hybrid Compounds

Shynggys Zhumagali

This certifies that the thesis of Shynggys Zhumagali is approved.

06. 27. 2019

Advisor: Kwang S. Kim

Bong Soo Kim: Thesis Committee Member #1

Oh-Hoon Kwon: Thesis Committee Member #2

Solid-State Synthesis of Low Dimensional Lead-Free Mn-based Fluorescent Organic-Inorganic Hybrid Compounds

Shynggys Zhumagali, Kwang S. Kim*

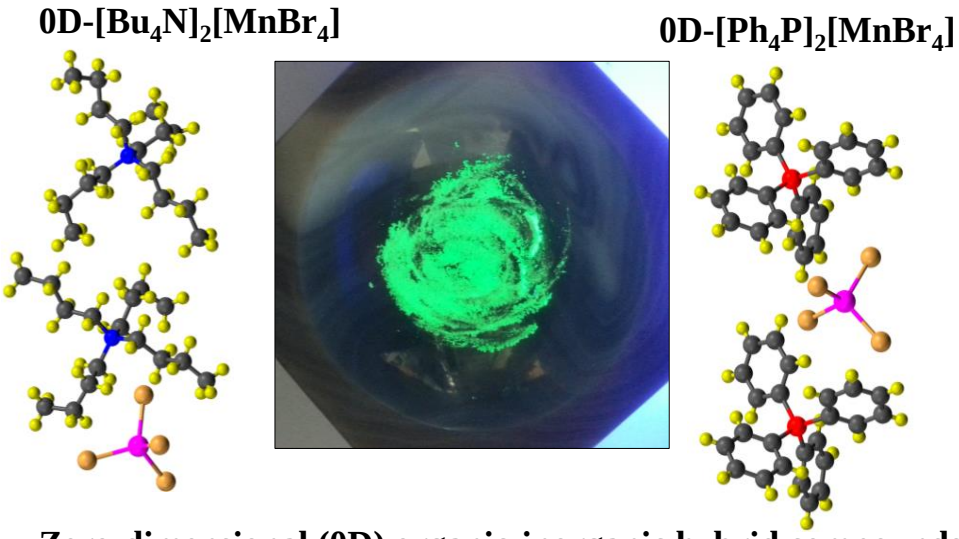

Zero-dimensional (0D) organic-inorganic hybrid compounds

ABSTRACT: We report the first solid-phase gram-scale syntheses of range of low-dimensional lead-free Mn-based fluorescent organic-inorganic hybrid compounds, with a general formula of $[R_4Y]MnX_3$ and $[R_4Y]_2MnX_4$ (R = CH_3, C_2H_5, C_4H_9, C_6H_5; Y = N, P; X = Cl, Br). This has been achieved by mechanochemical grinding of the organic tetraalkyl halide with manganese (II) halides in the absence of any liquid reaction media. Solid-phase synthetic route has several advantages, in particular, in the synthesis of hybrid compounds with different molecular dimensionalities. During the mechanochemical synthesis process, the organic R_4Y^+ and inorganic Mn^{2+} cations co-crystallized together with halide anions in solid state, forming low-dimensional molecular assembly, where each individual metal centers are suspended in the matrix of organic cations. Mainly, the mechanochemical synthesis was applied to prepare 0D-$[Me_4N]_2MnCl_4$, 0D-$[Bu_4N]_2MnBr_4$, 0D-$[Ph_4P]_2MnCl_4$ with brilliant green fluorescence at 520 nm, and 1D- $[Me_4N]MnCl_3$ with bright orange fluorescence at 620 nm. Additionally, a range of similar compounds with varying organic substituents were prepared to show the scope of this methodology. The ground products exhibit emission phenomena upon exciting with both below and above band gap photons with high photoluminescence quantum yield (PL-QY), which is attributed to the individual tetrahedral manganese centers. These findings open a new path for development of highly fluorescent non-toxic hybrid compounds with remarkable photochemical properties.

Table of Contents

List of Figures

List of Tables

I. INTRODUCTION

Organic-inorganic hybrid perovskites with a general formula of ABX_3 (where A is an organic ammonium salt, B is a metal center, and X is a halide ion) have gained tremendous attention due to their attractive optoelectronic properties for various solid-state applications, such as solar cells,[1] sensors,[2] quantum dots,[3] and lasers.[4] Among various perovskite materials, lead-halide perovskites have been the most prominent, due to their superior optoelectronic properties and efficiency. To date, lead-based perovskite materials show the highest power conversion efficiency (PCE) of more than 23% in the most recent reports,[5] which is the closest to its theoretical efficiency of 30%. Moreover, their various solid-state light emitting applications[5] have recently emerged due to the fabrication of zero dimensional (0D) perovskite-related compounds and other low dimensional lead perovskites.[6] However, despite their outstanding performance, lead-containing compounds are toxic[7] and cannot be utilized in the mass production of solar panels, or in bioapplications, such as sensors and imaging tools. Such drawbacks of lead-based perovskite materials outshadow their outstanding performance. So there is an urge for ecofriendly materials which give bright fluorescence in solid state. Therefore, environmentally friendly substitutes for lead-halide perovskites that can match the performance of the original perovskite material are still in demand. There are several alternatives for lead in the organic-inorganic hybrid perovskites, but not many of them are explored to depth to understand their optical behavior and try to implement in more practical applications. One of such materials are manganese (Mn) based organic-inorganic hybrid materials and photoluminescent complexes. Zink et al.[8] and Cotton et al.[9] have worked in 1960 and 1970 on fluorescent hybrid Mn complexes. But, these materials have never been explored exclusively as compared to lead based perovskite compounds.

Fluorescent tetrahedral manganese (II) complexes have been around for few decades, from the first synthesis by Cotton et al. in early 1960s. However, photoluminescent properties of manganese (II) compounds have not been getting proper attention. The emission in manganese perovskites takes place due to d-d transition in the metal center, which is strongly correlated with crystal field effect.[9] Therefore, the photoluminescence of manganese based complexes can be tuned to some extend by varying the coordination environment of the metal center. In this approach, Mn(II) complexes were observed to possess pressure-dependent PL, which is associated with the change in configuration from four-coordinated to five or six-coordinated modes upon increasing the pressure.[8] They can also show excellent triboluminescent properties, where cracking crystals of a material generates PL.[10] Typically, manganese (II) complex salts with tetrahedral configuration have brilliant green emission centered at 520 nm, while octahedral Mn(II) salts exhibit orange colored emission at 620 nm.[11] Additionally, unlike typical perovskite crystals, where the PL highly depends on the crystallinity of the bulk material, the tetrahedral Mn(II) complexes are zero-dimensional (0D) fluorophores with photoluminescent properties at the molecular level.[12] These 0D fluorophores have

discrete metal centers surrounded by organic cations and exhibit quantum confinement phenomena as the size of metal center falls in nanoregime. As the syntheses of 0D bulk crystals do not require any capping ligands, these materials will retain its high PL-QY during thin film device fabrication. Such low-dimensional perovskites have gained tremendous attention due to their exciting optical properties.[6b, 13]

In these work, we focus on the solid-state synthesis of various low-dimensional Mn-based organic-inorganic hybrid compounds with prominent photoluminescent properties. The solid-state synthesis employs mechanical grinding of precursor salts, tetraalkylammonium halide and manganese (II) halide, in stoichiometric ratio to provide mechanical and thermal energy sufficient enough for rearrangement of anions and cations in the precursors.[14] The crystalline structure of the 0D hybrids prepared by this method is composed of individual tetrahedral metal centers surrounded by organic cation, while 1D hybrid materials are composed of long chains of octahedrally coordinated photoluminescent metal centers bridged together by halide ions surrounded by organic cations.[14b] In lead-halide perovskites, the 0D perovskites preparation methodologies require precise control of the reaction conditions, use exact precursor amounts, and employ tedious processes which may be too long to perform.[15] Even then, it is unavoidable to have different 2D and 3D phases. Conversely, solid state synthesis employed in our work results in 100% yield of 0D material within 10 minutes, and less control is required. Additionally, they have better reproducibility, since their PL depends solely on the coordination environment of the metal center. Such methodology is important for device fabrication based on thin film solid state synthesis. Moreover, the chemical composition of the hybrid materials can be easily tuned by altering the stoichiometry of the precursors. Such manipulations not only can alter the dimensions of the final product, but also result in tuning of the band gap of the material and subsequently its photoluminescence range.[16] Such facile method of preparation of low-dimensional photoluminescent organic-inorganic hybrid materials can be utilized in fabrication of thin film devices for solid-state applications. Herein, several derivatives of Mn-based photoluminescent hybrid compounds with similar structure, such as $[R_4N]MnX_3$ and $[R_4Y]_2MnX_4$ (R = CH_3, C_2H_5, C_4H_9, C_6H_5; Y = N, P; X = Cl, Br), were prepared through the solid-state synthesis, and characterized for physical, chemical, and photoluminescent properties.

II. EXPERIMENTAL METHOD & MATERIALS

2.1. Materials

Tetramethylammonium chloride (Me_4NCl, ≥98.0%, MW 109.60), Tetraethylammonium chloride (Et_4NCl, ≥98.0%, MW 165.70), Tetrabutylammonium chloride (Bu_4NCl, ≥97.0%, MW 277.92), Tetraphenylphosphonium chloride Ph_4PCl, ≥98.0%, MW 374.84), Tetramethylammonium bromide (Me_4NBr, ≥98.0%, MW 154.05), Tetraethylammonium bromide (Et_4NBr, ≥98.0%, MW 210.16), Tetrabutylammonium bromide (Bu_4NBr, ≥99.0%, MW 322.37), Tetraphenylphosphonium bromide (Ph_4PBr, 97%, MW 419.29), Manganese(II) Bromide ($MnBr_2$, ≥99%, MW 214.75), Manganese(II) chloride ($MnCl_2$, ≥97.0%, MW 125.84), and ethanol were purchased from Sigma-Aldrich.

Synthesis of powder 0D-$[Me_4N]_2[MnCl_4]$

Me_4NCl (219.2 mg, 2 mmol) and $MnCl_2$ (125.8 mg, 1 mmol) were ground together using mortar and pestle for 10 minutes. The obtained light green powder, with brilliant green fluorescence under UV light, was dried under vacuum at 60 ˚C for 4 h. The resulting dry yellow green powder was used for further studies.

Synthesis of powder 1D-$[Me_4N][MnCl_3]$

Me_4NCl (219. mg, 2 mmol) and $MnCl_2$ (251.6 mg, 2 mmol) were ground together using mortar and pestle for 10 minutes. The obtained light pink powder, with bright orange fluorescence under UV light, was dried under vacuum at 60 ˚C for 4 h. The resulting dry pink powder was used for further studies.

Synthesis of single crystal 0D-$[Bu_4N]_2[MnBr_4]$

Bu_4NBr (644.7 mg, 2 mmol) and $MnBr_2$ (214.8 mg, 1 mmol) were dissolved in ethanol (5 ml) and then stirred for 10 minutes. The solution was filtered to obtain a clear solution and kept it for evaporation. After few days, light yellow color crystals formed. The crystals were kept in the mother liquor before performing single crystal X-ray analysis. The crystals exhibited bright green fluorescence under UV light.

2.2. Characterization Methods

The powder X-ray diffraction (PXRD) was done on D/MAX2500V/PC diffractometer (Rigaku) using Cu-rotating anode x-ray. The Bragg's diffraction angle (2θ) range was 5-50˚ with a scan rate of 2˚/ minute. The diffraction patterns were presented after baseline correction.

Single crystal X-ray diffraction (XRD) analyses were performed at Wester Seoul center of KBSI. A crystal was picked up with paratone oil and mounted on a Bruker D8 Venture PHOTON 100 CMOS diffractometer equipped with graphite-monochromated Mo Kα (λ= 0.7107Å) radiation source at 25 °C. The goniometer equipped with the diffractometer is KAPPA four circle goniometer with φ, κ,

ω and 2θ axes by which the crystal was rotated. The unit cell parameters were determined by collecting the diffracted intensities from 24 frames measured in two different crystallographic zones and using the method of difference vectors. Data collection and integration were carried out with SMART APEX2 (Bruker, 2012) and SAINT (Bruker, 2012). Absorption correction was done by multi-scan method implemented in SADABS. The crystal structures were solved by direct methods and refined by full-matrix least-squares on F^2 using SHELXTL. All the non-hydrogen atoms were refined anisotropically, and hydrogen atoms were added to their geometrically ideal positions.

X-ray photoelectron spectra (XPS) of powder samples were taken using X-ray photoelectron spectrometer of K-alpha model (ThermoFisher).

Thermogravimetric analysis (TGA) was performed using Q500 model, TA.

Scanning electron microscopy (SEM) images were taken using SU8220 Cold FE-SEM (Hitachi High-Technologies).

Fourier-transform infrared spectra (FTIR) were collected in FTIR model 670-IR (Varian) with attenuated total reflection detector.

The optical differential reflectance spectra (DRS) of all solid samples were recorded using a Cary 5000 UV-Vis-NIR Spectrophotometer (Agilent), with integrated sphere in diffuse-reflectance mode to collect UV-Vis diffuse reflectance spectra, and then to converted it into Kubelka-Munk function, F(R).

Photoluminescence (PL) spectra of Mn complexes were collected using Cary Eclipse fluorometer (Varian) in a powder measurement mode.

Photoluminescence quantum yield (PLQY) has been experimentally evaluated using FP-8500ST Spectrofluorometer (Jasco International). PLQY has been evaluated by integrating sphere and the following equations have been used:

Quantum yield [%] = $S_2/(S_0-S_1)$ ×100 (S_1 = area scattered from the sample, S_2 = area emitted from sample, S_0 = area from incident light with blank sample holder.)

The photoluminescence single particle imaging of powder samples were taken in LSM 780 NLO (Carl Zeiss). The focus of the samples was adjusted mechanically using 10 × air and 100 × oil objective lenses, with the excitation laser source of 405 nm. The detection range was 420-700 nm (8.9 nm).

2.3. Computational Methods

Density functional theory calculations were performed by first-principles calculation in the framework of density functional theory (DFT) calculations using the plane-wave formalism as implemented in the Vienna ab-initio simulation package (VASP).[17] We use the generalized gradient approximation (GGA) and Perdew–Burke–Ernzerhof (PBE)[18] augmented by including Hubbard-U corrections (GGA+U) based on Dudarev's approach[19]. In Dudarev's approach, the Coulomb and exchange interactions are specified by the U_{eff} parameter. The core–valence interaction is described by the projector-augmented wave method. We have also considered the Tkatchenko–Scheffler method[20] for dispersion correction. Plane wave functions were expanded with an energy cutoff of 520 eV and Brillouin zone sampled using 4×4×4 gamma centered k-mesh. The value of U_{eff} = 4 eV is used for Mn atom to treat strong correlation Mn-3*d* electrons.[21] Structure optimization was performed on full unit cell of **1** and **2** containing 444 and 380 atoms, respectively. All atoms are fully relaxed using the conjugate-gradient method until the absolute values of the Hellman–Feynman forces were converged to within 0.0025 eV/Å.

III. RESULTS AND DISCUSSION

3.1. 0D-$[Me_4N]_2[MnCl_4]$ and 1D-$[Me_4N][MnCl_3]$

3.1.1. Physical and chemical characterization

For the first time, the synthesis of 0D-$[Me_4N]_2[MnCl_4]$ (**1**) and 1D-$[Me_4N][MnCl_3]$ (**2**) was performed in a single step through mechanochemical grinding of $(CH_3)_4NCl$ and $MnCl_2$ in mortar followed by drying of the obtained hybrids under vacuum at 60 ˚C for 6 h. During the synthesis, the amounts of organic and inorganic components were altered to get 0D hybrid with 2:1 ratio and 1D hybrid with 1:1 ratio. The synthesis process resulted in two luminescent hybrid compounds with different fluorescent properties. Mainly, **1** showed bright green fluorescent under 365 nm UV lighting, while **2** possessed bright orange fluorescence. The photography images of both **1** and **2** are shown on the figure 1.

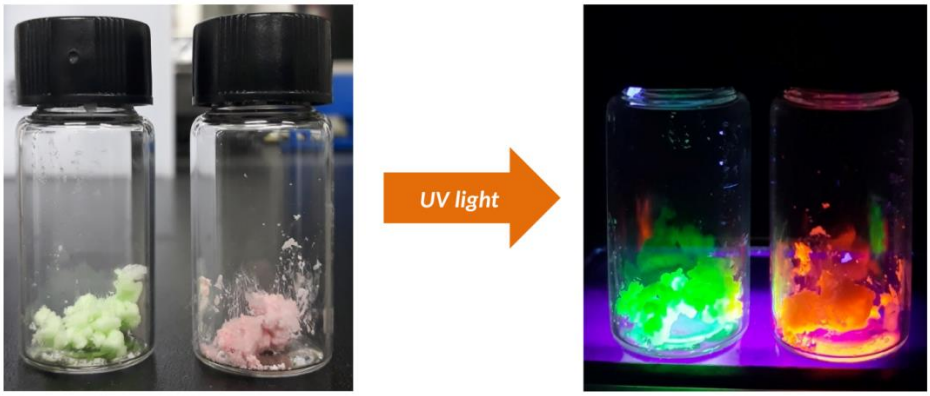

Figure 1. Photography images of **1** and **2** under indoor lighting and UV lighting.

Following the one-step synthesis, the phase purity of obtained hybrids was determined. Powder XRD pattern of both **1** and **2** match their single crystal XRD patterns obtained from single crystal X-ray analysis (Figure 2).[22] The crystal structure of **1** consists of isolated tetrahedral $MnCl_4^{2-}$ species surrounded by tetramethylammonium cations (Figure 3a), while **2** has a linear structure with octahedral metal centers bridged by face-sharing three chloride anions suspended in the pool of tetramethylammonium cations (Figure 3b). The presence or absence of certain functional groups was assessed by FT-IR measurements (Figure 4a). The compounds possess similar IR spectra, with a broad peak at 3398 cm^{-1} for O-H stretching, mainly due to its hygroscopicity when kept under ambient environment for long time. Even after thorough drying under vacuum, the sample absorbs little amount of moisture from air, which could affect the FT-IR results, but it does not affect the photoluminescent properties of hybrids. Both **1** and **2** possess small peak at 3030 cm^{-1} for alkyl C-H stretch present in the tetramethylammonium moiety. They also possess H-C-H bending at 1483 cm^{-1}

characteristic for alkyl moiety. Apart from the peaks essentially present in **1** and **2**, FT-IR analyses do not contain foreign peaks, which confirm the purity of the final products. This is indeed the case, because the synthesis was performed from pure precursor salts with 100% conversion.

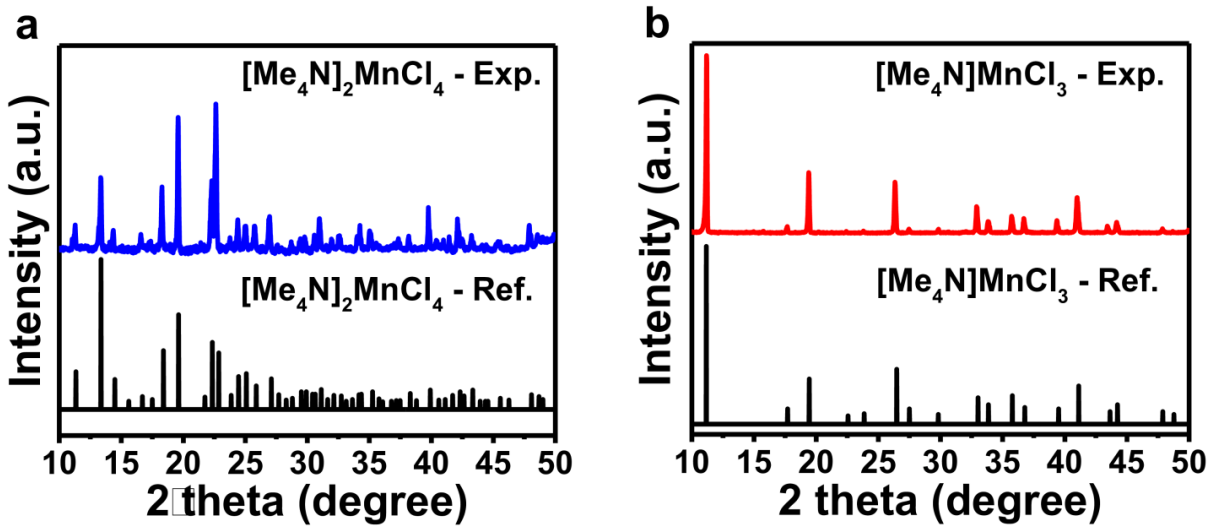

Figure 2. Powder XRD patterns of (a) **1** and (b) **2** with their reference spectra obtained from single crystal XRD measurement database.

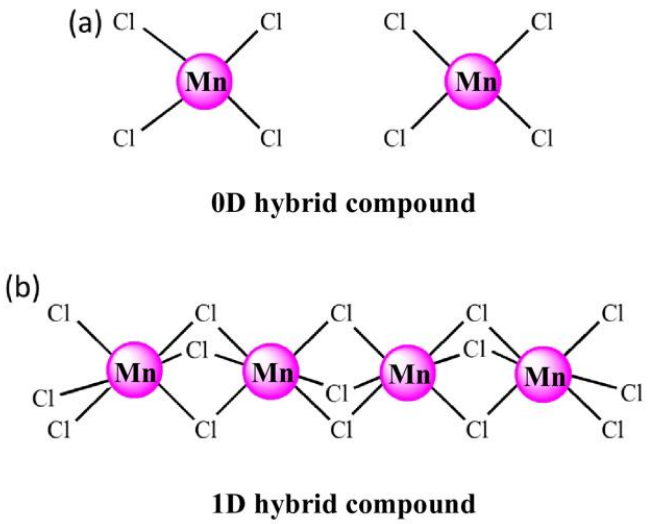

Figure 3. Simplified crystal structures and location of metal centers in (a) 0D and (b) 1D-hybrid complexes.

The thermal stability of **1** and **2** was analyzed by thermogravimetric analysis (TGA) and by differential scanning calorimetry (DSC). Both **1** and **2** has a three-step decomposition profile, with 46.3% and 36.3% weight drop for **1**, and 63.4% and 24.6% weight drops for **2** (Figure 4b). Since the analysis was performed in ambient environment, the weight drops are accompanied by oxidation of

manganese, which makes it harder to interpret the data above 400 ˚C. However, from the TGA analysis, we can safely assume the stability of both compounds up to 400˚C, where a constant weight is maintained. A DSC analyses were performed in the stability range of **1** and **2** (Figure 5). The first endothermic scan for **1** contains a peak with onset at 143 ˚C, thus indicating a possible phase transition, i.e. melting (Figure 5a). The first exothermic scan possesses a peak with the similar intensity corresponding to crystallization of the material. The second endothermic scan contains the same melting peak, but at lower temperature. Similar phenomenon is observed with compound **2**, but with less prominent melting and crystallization peaks (Figure 5b). The DSC analysis confirms the stability of **1** and **2** up to 400 ˚C, with reversible melting and crystallization points at around 143 ˚C for **1**, and 135 ˚C for **2**.

The surface chemistry of **1** and **2** was analyzed by X-ray photoelectron spectroscopy (XPS) measurements (Figures 6-8). A wide scan XPS survey contains prominent peaks for Mn 2p, O 1s, N 1s, C 1s, Cl 2p (Figure 6). The Mn 2p spectra of **1** in figure 7a possess two peaks at 643 eV and 655 eV, corresponding to $2p_{3/2}$ and $2p_{1/2}$ transitions.[23] The peaks are sharp, which is associated with only Mn(II) species present in the sample. The deconvolution of Cl 2p spectra for **1** result in characteristic peaks of metal-bound chlorine at 197 eV and 199 eV for $2p_{3/2}$ and $2p_{1/2}$ transitions, as well as another chlorine environment bound to more electronegative species, most likely oxygen, at 202.5 eV and 204 eV. (Figure 7b). As stated earlier both **1** and **2** have hygroscopic properties, which makes them absorb moisture from the air very quickly. In the presence of moisture and air, the chloride atoms present in both precursor salts tend to oxidize into chlorates. The deconvolution of two broad peaks in C 1s spectra of **1** in Figure 7c reveals the presence of two different carbon environments, (i) C atoms bound to N atoms with lower binding energy of 1s electrons (285 eV), and (ii) C atoms bound to more electronegative O atom with slightly higher 1s electron binding energy (289 eV). As stated above, the absorption of carbon dioxide, moisture, and oxygen from air results in the formation of carbonates and other oxidized species. To support this assumption, N 1s XPS spectra also contains two different environments, with 1s electrons originating from nitrogen in tetramethylammonium (402 eV), and 1 s electron bound to more electronegative oxygen atom in nitrates (406 eV). The XPS spectra of Mn 2p and Br 3d for **2** are similar to the XPS spectra of **1** (Figure 8a). Similarly, C 1s spectrum possesses two peaks corresponding to C-N bonding in tetramethylammonium at 285 eV and C-O bonding in carbonate at 288 eV (Figure 8c). The N 1s spectrum of **2** is similar to XPS spectra of **1**, with two peaks for tetramethylammonium and nitrate moieties. The elemental and oxidation state purity of both **1** and **2** are confirmed by the XPS analysis.

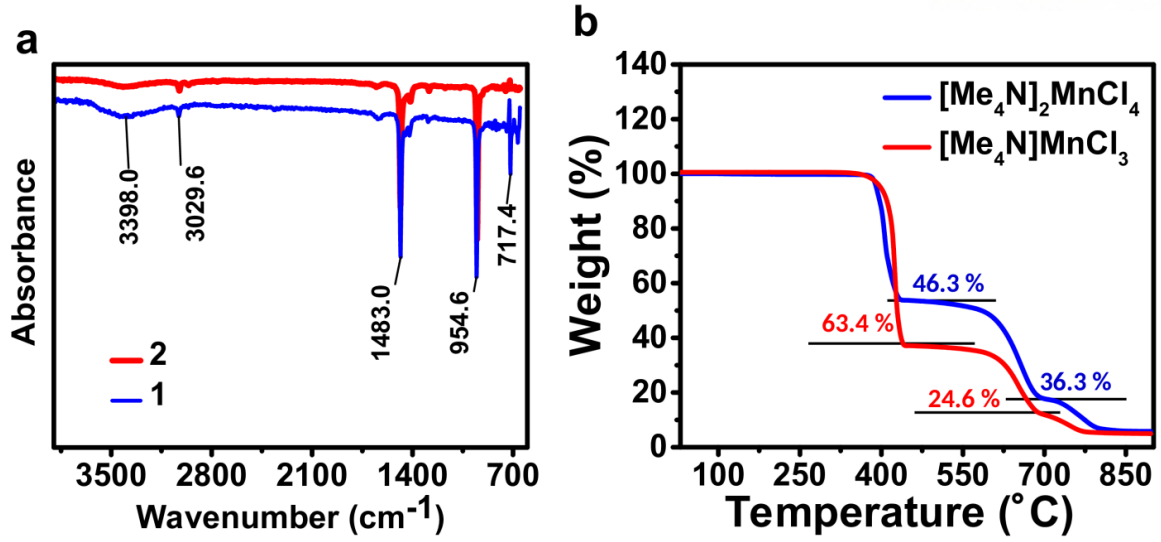

Figure 4. (a) FT-IR measurements of **1** and **2**, and (b) stability check by TGA

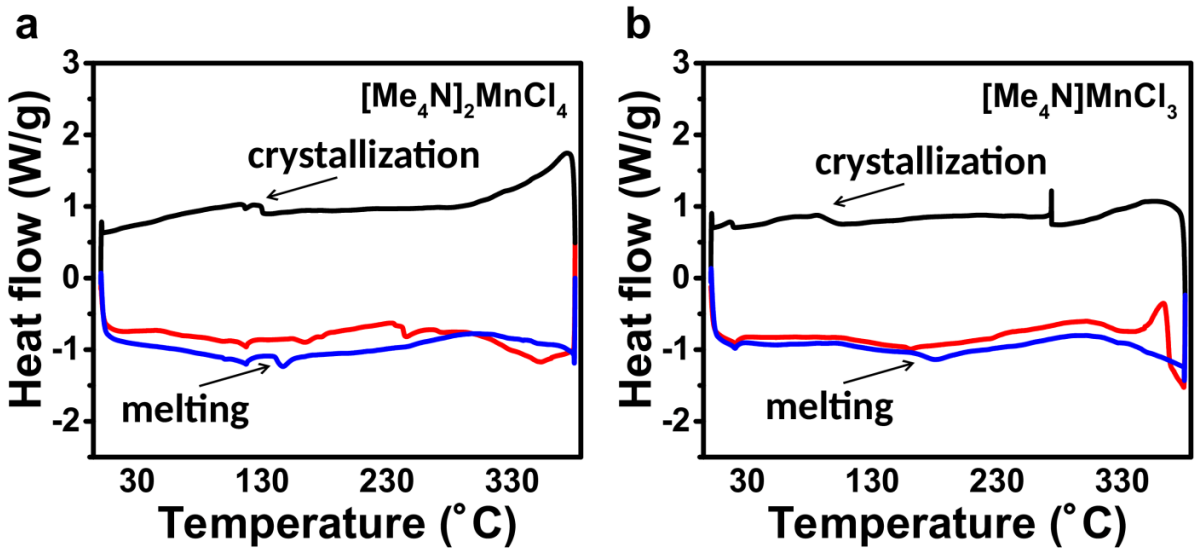

Figure 5. (a-b) DSC analysis of **1** and **2** with the first forward scan (red), the first backward scan (black), and the second forward scan (blue).

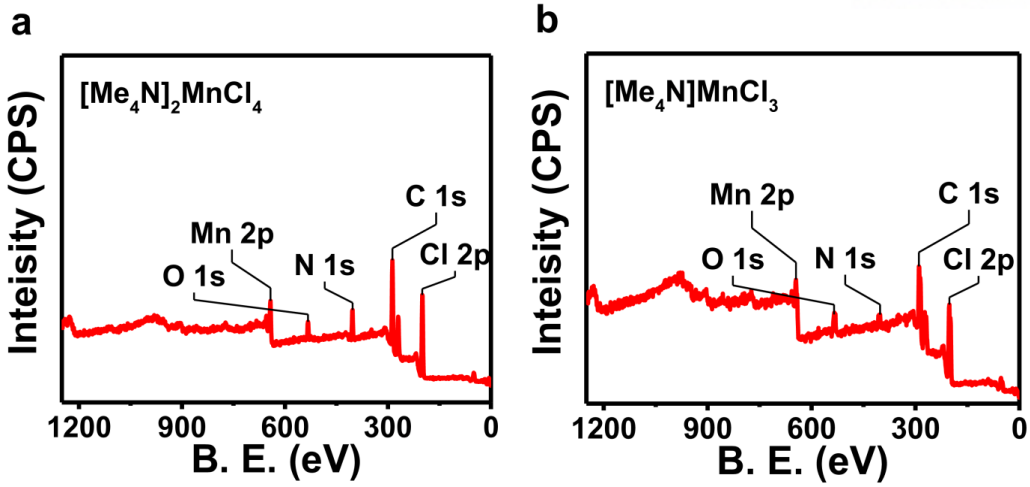

Figure 6. Wide scan XPS survey data of (a) $[Me_4N]_2MnBr_4$ and (b) $[Me_4N]MnBr_3$ at ambient environment.

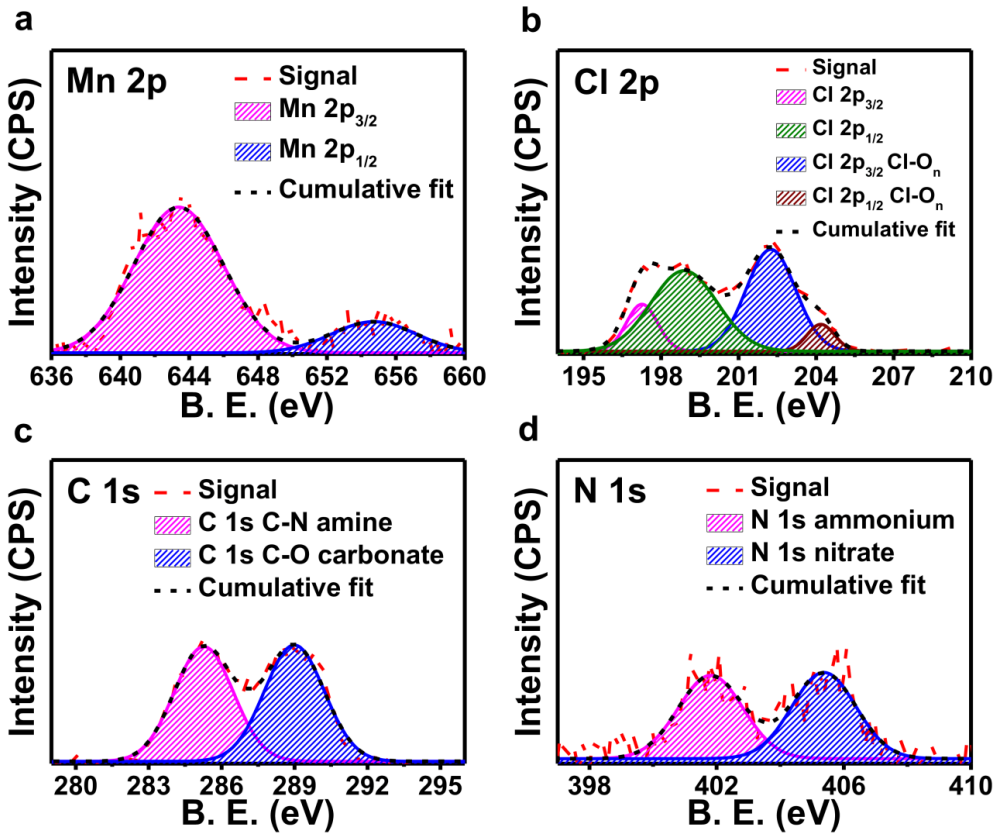

Figure 7. High resolution XPS scans of $[Me_4N]_2MnBr_4$ for (a) Mn 2p, (b) Cl 2p, (c) C 1s, and (d) N 1s.

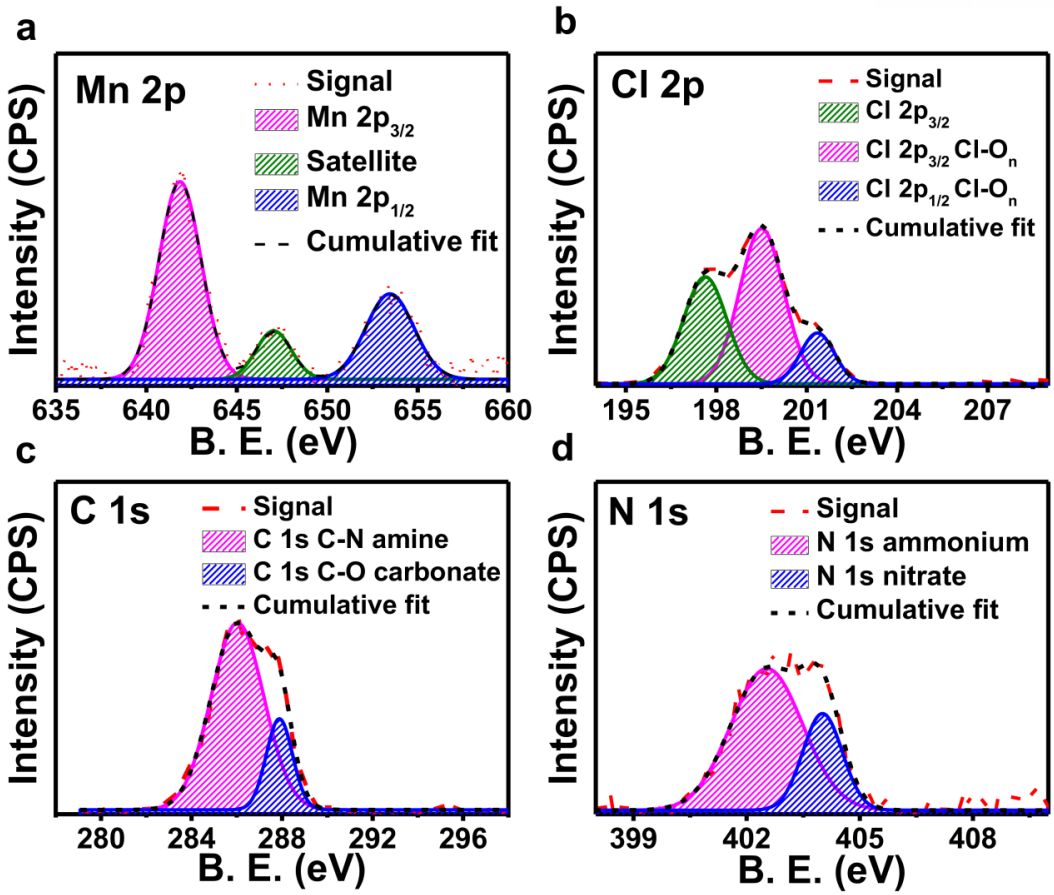

Figure 8. High resolution XPS scans of $[Me_4N]MnBr_3$ for (a) Mn 2p, (b) Cl 2p, (c) C 1s, and (d) N 1s.

3.1.2. Photochemical properties

To explore the photophysical properties of these compounds, solid-state diffusion reflectance spectra (DRS) and photoluminescence (PL) analysis were performed (Figure 9).[24] The absorption spectra of **1** exhibits peaks at 2.65, 2.77, 2.87, 3.26, 3.38 and 3.46 eV which corresponds to the transition from ground state $^6A_1(S)$ to $^4T_1(G)$, $^4T_2(G)$, $^4A_1$, $^4E(G)$, $^4T_2(D)$, $^4E(D)$, $^4T_1(P)$, respectively. The **2** shows absorption peaks at 2.33, 2.79, 2.95, 3.35, 3.48, 3.79 eV which is associated with $^4T_{1g}$ (G), $^4T_{2g}$ (G), $^4A_{1g}$, ^4E_g (G), $^4T_{2g}$ (D), ^4E_g (D), $^4T_{1g}$ (P) excited states. The band gaps of **1** and **2** were determined by plotting $[F(R)eV]^2$ versus eV, and constructing estimating x-intercepts of each line that follows the slope of each peak (Figure 10). This results in **1** having a band gap of about 2.4 eV and **2** having a band gap of around 2.15 eV. The drastic change in PL behavior is observed in between 0D **1** and 1D **2**. Mainly, **1** exhibits a PL peak in green region (2.37 eV), while **2** possesses fluorescence in red region (2.00 eV). This difference is attributed to the crystal field splitting of tetrahedral and octahedral geometry of Mn complexes. The crystal field splitting energy for tetrahedral complex is lower than the octahedral complex and consequently, the first $^4T_1$ emitting excited state in tetrahedral resides above the $^4T_{1g}$ in octahedral. This is the reason for shifting of PL band gap in 0D-$[(CH_3)_4N]_2MnCl_4$ and 1D-$(CH_3)_4NMnCl_3$. It is interesting to note that only the variation in amount of

ammonium organic cations allowed the band gap shift from green to red region. This kind of phenomena is not observed in case of 0D and 1D halide perovskites. Despite its excellent photoluminescent activity, organic-inorganic hybrids 1 and 2 have moderate stability under extreme conditions, and can facilely decompose under the influence of moisture and air. Therefore, the composition of the hybrids can be tuned, to enhance their stability without sacrificing photoluminescent properties.

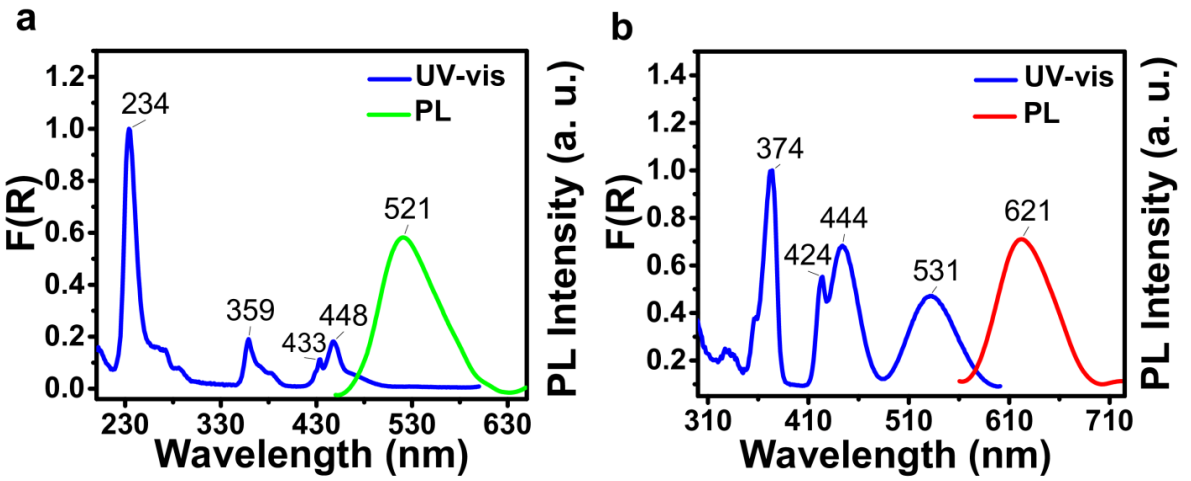

Figure 9. Solid-state diffusion reflectance spectra and PL spectra for compounds (a) **1** and (b) **2**.

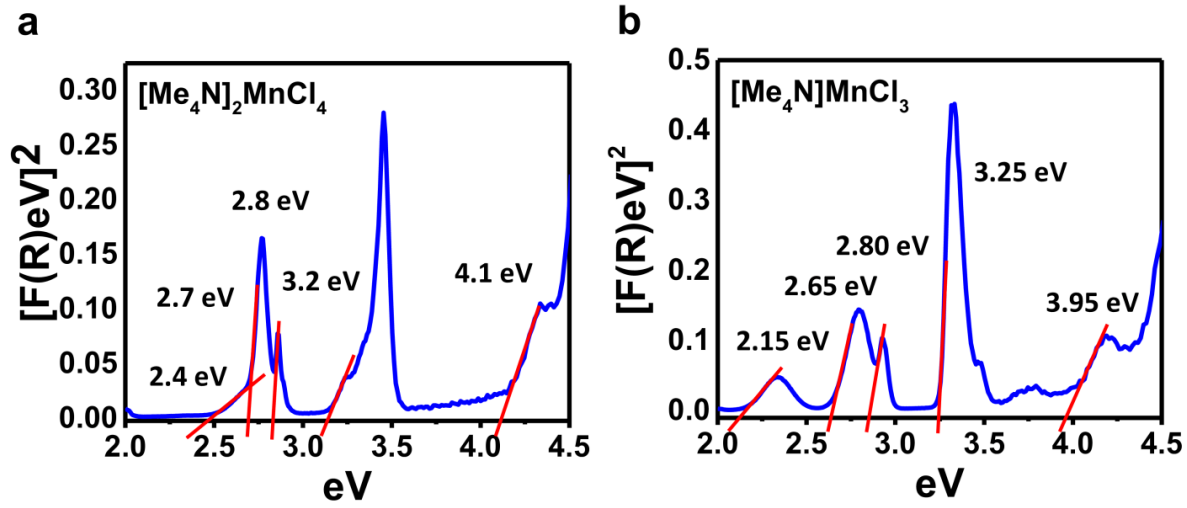

Figure 10. $[F(R)\bullet eV]^2$ vs. eV plot for determination of band gap of (a) **1** and (b) **2**.

3.2 0D-$[Bu_4N]_2[MnBr_4]$ and 0D-$[Ph_4P]_2[MnBr_4]$

3.2.1. Physical and chemical characterization

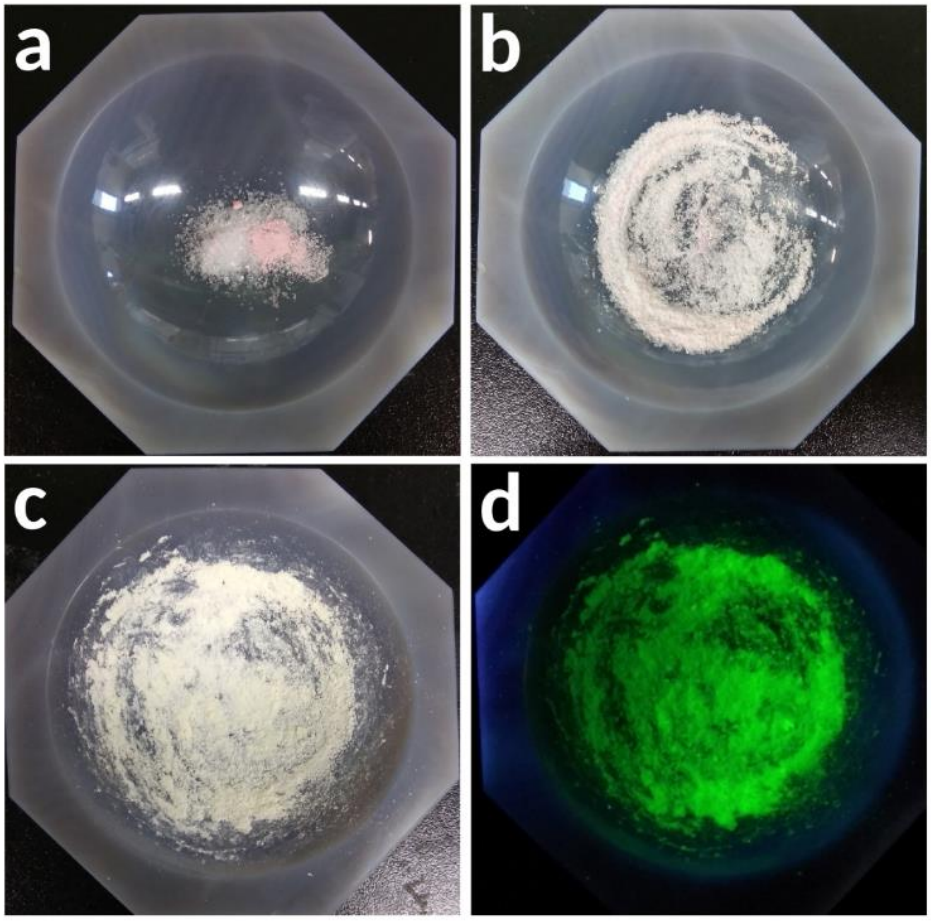

Figure 11. Photography images of $[Bu_4N]_2MnBr_4$ at different stages of synthesis: (a) two precursors before grinding; (b) two precursors after mixing for 5 min; (c) final product after grinding for 10 min; (d) final product under 365 nm UV irradiation.

The organic-inorganic hybrids **1** and **2** discussed previously have excellent photoluminescent properties however their chemical stability suffered from hygroscopicity. Obtained materials tend to absorb moisture from the atmosphere if left exposed for few hours, which facilitated the partial decomposition of the compounds. Even though the partial decomposition has no effect on the photoluminescent properties of hybrids, it could potentially jeopardize their overall stability on a long term. Therefore, more robust and stable alternatives, with similar photochemical properties, were required. This was achieved by switching the methyl substituent in the organic cation to more bulky butyl or phenyl groups. In each case, the primary alkyl substituent was replaced by less reactive secondary alkyl or aromatic substituents. To complement for the size difference of the methyl and butyl substituents, the chloride counterpart was switched to bromides. The syntheses of

$[Bu_4N]_2[MnBr_4]$ (**3**) and $[Ph_4P]_2[MnBr_4]$ (**4**) were performed by the same mechanochemical reaction using mortar and pestle. During this process, the crystalline structure of $MnBr_2$ was broken by means of thermal and mechanical energy provided by grinding, and the vacant sites on the metal center are coordinated by two more Br atoms from the organic precursor salt. Negative charge in tetrahedral $[MnBr_4]^{2-}$ is neutralized by two ammonium cations, which results in isolated 0D photoluminescent particles surrounded by organic moiety.[14b] Photography images on the figure 11 illustrate different stages in the preparation of compounds **3** and **4**. The two precursor salts are initially mixed in a mortar, followed by intensive grinding for 10 minutes. As a result, fluorescent Mn-based organic-inorganic hybrids are formed. From the SEM images on the figures 12-13, the prepared hybrids **3** and **4** have irregular morphology, with no distinctive crystalline structure.

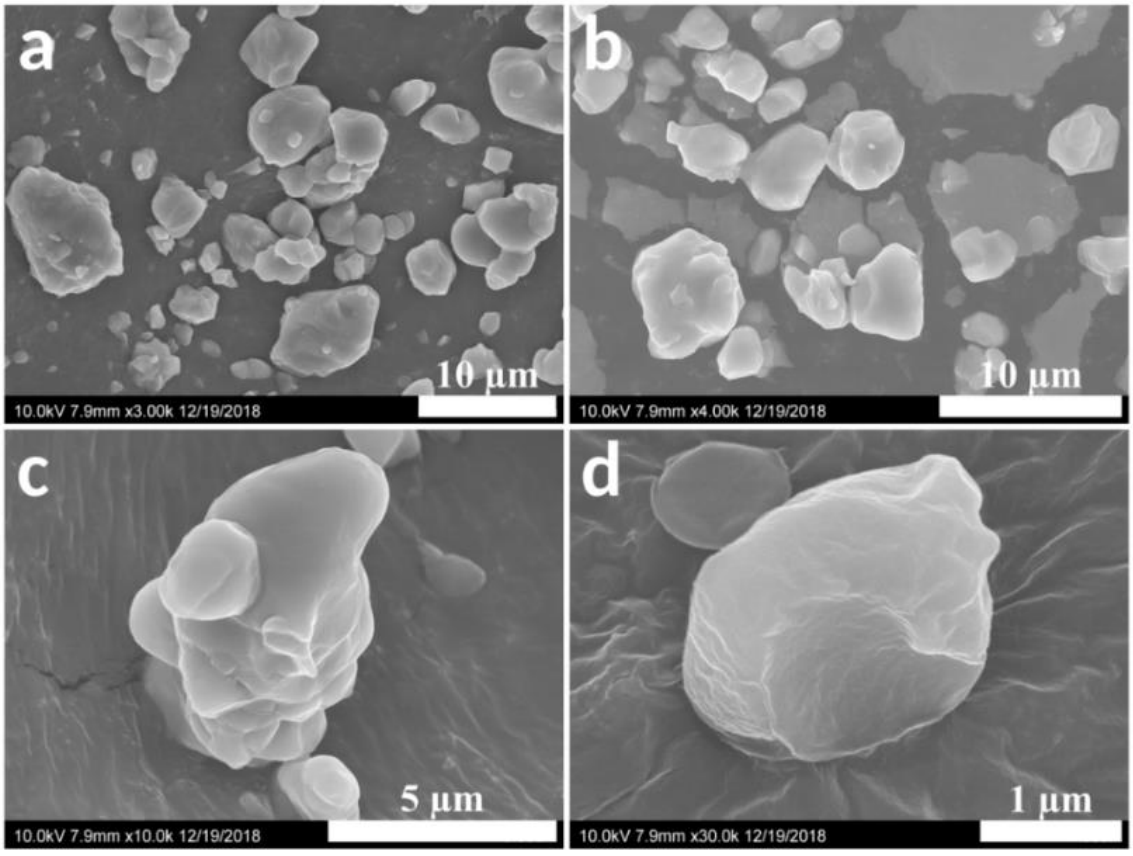

Figure 12. SEM images of $[Bu_4N]_2MnBr_4$ at (a-b) low magnification with particle distribution, and (c-d) single particle images at high magnification.

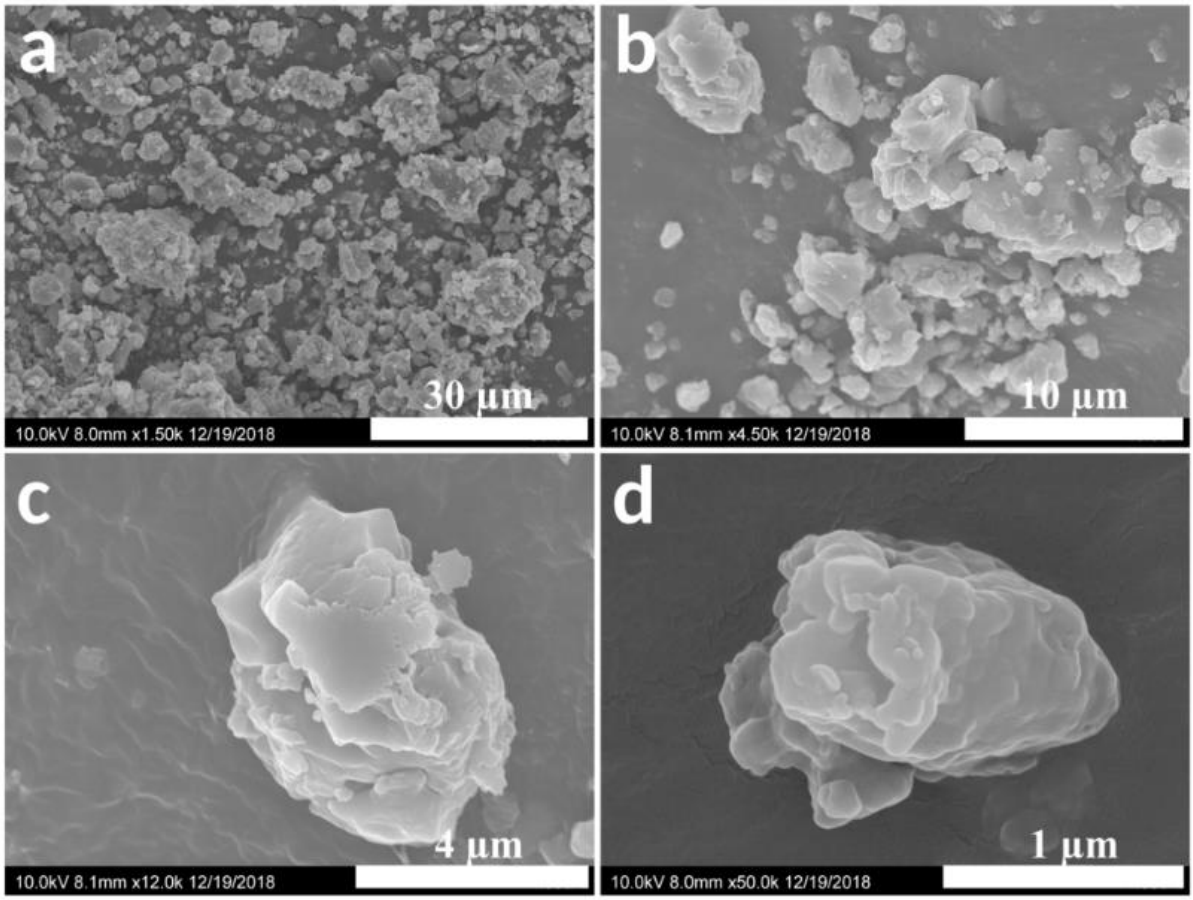

Figure 13. SEM images of $[Ph_4P]_2MnBr_4$ at (a-b) low magnification with particle distribution, and (c-d) single particle images at high magnification.

Phase purity of the obtained photoluminescent compounds was confirmed by powder X-ray diffraction (PXRD) analysis (Figure 14). Single crystals of both **3** and **4** were grown through solution assisted synthesis, where ethanolic solutions of precursors were slowly evaporated over 5 days until the crystals of **1** and **2** were obtained. According to single crystal XRD measurements in tables 1 and 2, compound **3** has an orthorhombic crystal structure with $P2_12_12_1$ space group, while **4** has a monoclinic crystal structure with C2/c space group. The unit cells of **3** and **4** are shown in the figure 15. The metal centers of both compounds have distorted tetrahedral geometry, with bond length between 2.505 Å and 2.517 Å. The Mn^{2+} cations in **3** and **4** possess tetrahedral geometries, with C-N bond lengths between 1.437 Å and 1.550 Å for **3**, and C-P bond lengths between 1.783 Å and 1.800 Å for **4** (Tables 3, 4). The powder XRD patterns of both complexes are well-matched to single crystal XRD spectra of the corresponding compounds, with slightly varying intensities, due to non-uniform crystallinity of the powder samples. The calculated unit cells of both **3** and **4** are shown on the figure 15, with the corresponding dimensions. Figure 14b shows the FT-IR spectra of **3**, which exhibits characteristic peaks for saturated hydrocarbon, with symmetric/ asymmetric C-H stretching at 2871

cm^{-1} /2958 cm^{-1}, and C-H and H-C-H bendings at 1376/1485cm^{-1}. **4** possesses weak peaks for aromatic C-H/ C=C stretchings at 3055/1585cm^{-1} and C-H bending at 1107 cm^{-1}. Both compounds have only characteristic vibrations, with no sign of impurities.

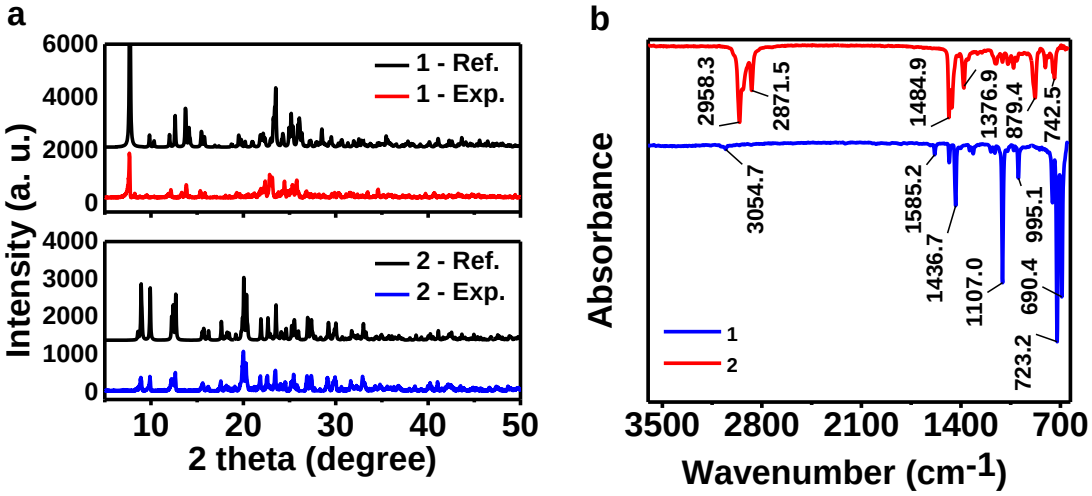

Figure 14. Physical Characterizations. (a) Powder XRD patterns of **3** and **4** with their reference spectra obtained from single crystal XRD measurements; (b) FT-IR absorption spectra of **3** and **4**.

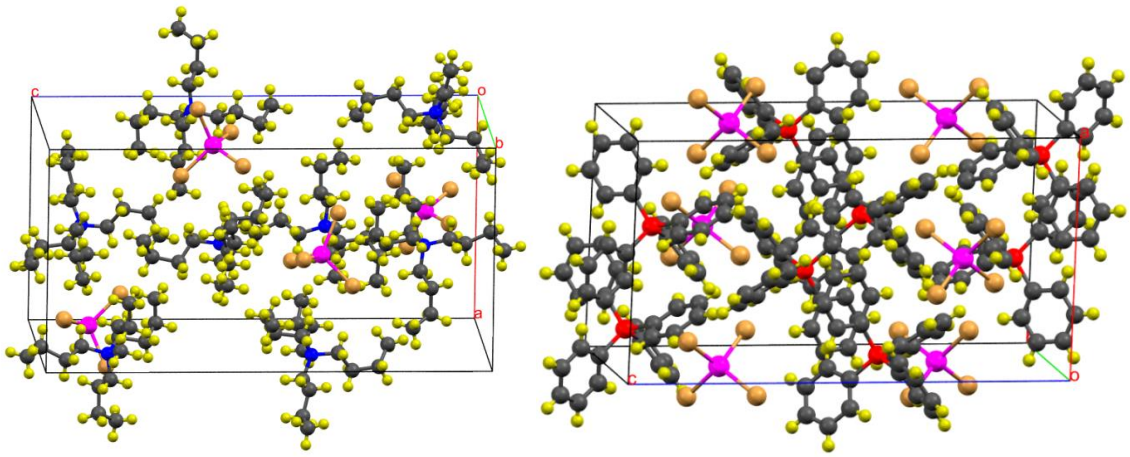

Figure 15. Unit cell of **3** (left) and **4** (right) (Pink = Mn, Yellow = H, Blue = N, Red = P, Orange = Br).

Table 1. Crystal data and structure refinement for $[Bu_4N]_2MnBr_4$.

Parameter	Value
Identification code	$[Bu_4N]_2MnBr_4$
Empirical formula	2(C16H36N)Br4Mn
Formula weight	859.49
Temperature	223(2) K
Wavelength	0.71073 Å
Crystal system	Orthorhombic
Space group	$P2_12_12_1$
Unit cell dimensions	a = 12.8381(7) Å α = 90°.
	b = 12.8997(8) Å β = 90°.
	c = 25.0820(15) Å γ = 90°.
Volume	4153.8(4) $Å^3$
Z	4
Density (calculated)	1.374 Mg/m^3
Absorption coefficient	4.186 mm^{-1}
F(000)	1772
Crystal size	0.280 x 0.210 x 0.150 mm^3
Theta range for data collection	2.238 to 28.385°.
Index ranges	-17<=h<=17, -17<=k<=17, -33<=l<=33
Reflections collected	140228
Independent reflections	10374 [R(int) = 0.0926]
Completeness to theta = 25.242°	99.9 %
Absorption correction	Semi-empirical from equivalents
Max. and min. transmission	0.7457 and 0.5105
Refinement method	Full-matrix least-squares on F^2
Data / restraints / parameters	10374 / 26 / 360
Goodness-of-fit on F^2	1.070
Final R indices [I>2sigma(I)]	R1 = 0.0662, wR2 = 0.1700
R indices (all data)	R1 = 0.0940, wR2 = 0.1824
Absolute structure parameter	0.055(5)
Extinction coefficient	n/a
Largest diff. peak and hole	0.586 and -0.450 e.$Å^{-3}$

Table 2. Crystal data and structure refinement for $[Ph_4P]_2MnBr_4$.

Parameter	Value
Identification code	$[Ph_4P]_2MnBr_4$
Empirical formula	C48H40Br4MnP2
Formula weight	1053.32
Temperature	293(2) K
Wavelength	0.71073 Å
Crystal system	Monoclinic
Space group	C2/c
Unit cell dimensions	a = 11.2817(3) Å α = 90°.
	b = 19.7797(6) Å β = 92.3422(10)°.
	c = 20.5926(6) Å γ = 90°.
Volume	4591.4(2) $Å^3$
Z	4
Density (calculated)	1.524 Mg/m^3
Absorption coefficient	3.870 mm^{-1}
F(000)	2092
Crystal size	0.220 x 0.170 x 0.100 mm^3
Theta range for data collection	2.079 to 28.311°.
Index ranges	-15<=h<=15, -26<=k<=26, -27<=l<=27
Reflections collected	74530
Independent reflections	5716 [R(int) = 0.0603]
Completeness to theta = 25.242°	100.0 %
Absorption correction	Semi-empirical from equivalents
Max. and min. transmission	0.7457 and 0.6043
Refinement method	Full-matrix least-squares on F^2
Data / restraints / parameters	5716 / 0 / 249
Goodness-of-fit on F^2	1.040
Final R indices [I>2sigma(I)]	R1 = 0.0393, wR2 = 0.0778
R indices (all data)	R1 = 0.0672, wR2 = 0.0909
Extinction coefficient	n/a
Largest diff. peak and hole	0.990 and -0.758 $e.Å^{-3}$

Table 3. Bond length [Å] of Mn-Br and C-N in $[Bu_4N]_2MnBr_4$.

Bond type	Bond length
Mn(1)-Br(4)	2.506(2)
Mn(1)-Br(3)	2.514(2)
Mn(1)-Br(2)	2.515(2)
Mn(1)-Br(1)	2.517(2)
N(1)-C(13)	1.473(17)
N(1)-C(1)	1.504(15)
N(1)-C(5)	1.526(16)
N(1)-C(9)	1.550(16)

Table 4. Bond length [Å] of Mn-Br and P-N in $[Ph_4P]_2MnBr_4$.

Bond type	Bond length
Mn(1)-Br(1)	2.5049(5)
Mn(1)-Br(1)#1	2.5049(5)
Mn(1)-Br(2)#1	2.5145(5)
Mn(1)-Br(2)	2.5146(5)
P(1)-C(13)	1.783(3)
P(1)-C(19)	1.787(3)
P(1)-C(1)	1.791(3)
P(1)-C(7)	1.800(3)

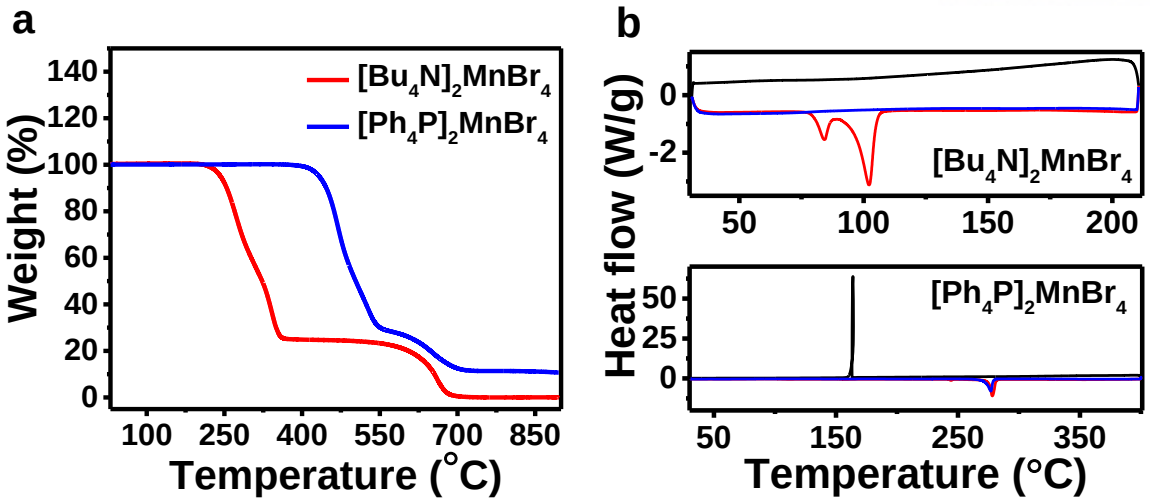

Figure 16. Physical Characterizations. (a) Thermal stability graphs of **3** and **4** obtained by TGA in inert atmosphere; (b) DSC measurements on powders of **3** and **4** and corresponding phase changes in their thermal stability interval for first forward scan (red), first backwards scan (black), and second forward scan (blue).

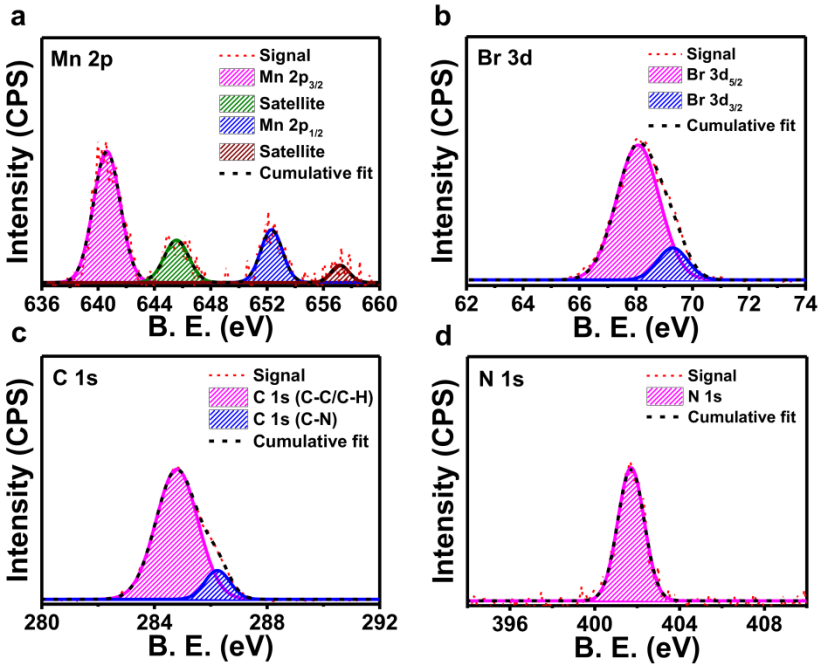

Figure 17. High resolution XPS scans of $[Ph_4P]_2MnBr_4$ for (a) Mn 2p, (b) Br 3d, (c) C 1s, and (d) P 2p.

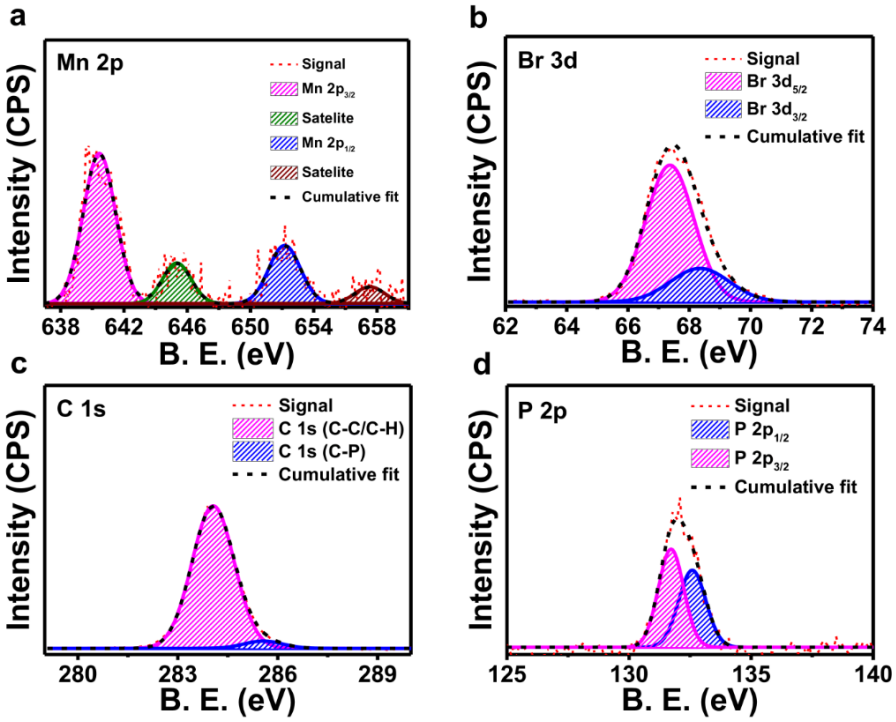

Figure 18. High resolution XPS scans of $[Ph_4P]_2MnBr_4$ for (a) Mn 2p, (b) Br 3d, (c) C 1s, and (d) P 2p.

The thermal stability and possible phase transitions were analyzed by TGA and DSC. Figure 16a contains the thermal stability curves of **3** and **4**. The decomposition of **3** starts after 220˚C, with two-step weight drops until complete decomposition above 700˚C. A DSC measurement in the stability range of **3** has a melting peak onset at above 60˚C during the first forward scan, with the melting point at 100˚C. However, no phase transitions occur for the reverse and second forward scan (Figure 16b). This indicates that **3** undergoes phase transition above 60˚C, and starts to irreversibly melt down above 100˚C. On the other hand, **4** has excellent stability up to 400˚C, with the melting and crystallization peaks in both forward and reverse DSC scans. The melting happens above 270˚C, while **4** is completely stable below 270˚C. This additional robustness might be inherent from the tetraphenyl phosphine cation, which is more constricted in its structure due to four aromatic rings in the moiety.

The surface chemistry of **3** and **4** was analyzed by X-ray photoelectron spectroscopy (XPS) measurements. Mn 2p spectra of **3** possess two peaks at 641 eV and 652 eV, corresponding to $2p_{3/2}$ and $2p_{1/2}$ transitions (Figure 17a).[23] The peaks are sharp, which is associated with only Mn(II) species present in the sample. It also contains satellite peaks at 646 eV and 657 eV.[23] The Br 3d spectra for **3** exhibits characteristic peaks of bromine at 68 eV and 69.5 eV for $3d_{5/2}$ and $3d_{3/2}$ transitions (Figure 17b), and N 1s transition appear at 402 eV (Figure 17d). The deconvolution of broad peak in C 1s spectra of **3** in Figure 18c reveals the presence of two different carbon

environments, (i) C atoms bound to another C atom with lower binding energy of 1s electrons (285 eV), and (ii) C atoms bound to more electronegative N atom with slightly higher 1s electron binding energy (286.5 eV). The XPS spectra of Mn 2p and Br 3d for **4** are identical with the XPS spectra of **3** (Figure 18). Similarly, C 1s spectrum possesses one broad peak with a small shoulder peak for C-C bonding at 284 eV and C-P bonding at 286 eV (Figure 18c). Transitions in P 2p spectra of **4** are deconvoluted into two peaks at 132 eV and 133 eV for $2p_{3/2}$ and $2p_{1/2}$, respectively (Figure 18d). The elemental and oxidation state purity of both **3** and **4** can be confirmed from the XPS analysis. According to the XPS analysis, both **3** and **4** have surface stability without any elemental oxidation state impurities. The compounds consist of only expected species, without any evidence of possible decomposition.

3.2.2. Photochemical properties

To analyze the photochemical properties, a solid-state diffusion reflectance (SSDR) analysis and PL measurements were carried out. Figure 19 shows the Kubelka-Munk (K-M) function of diffusion reflectance percentage for **3** and **4** as a function of wavelength.[24] The absorbance spectra of **3** exhibit peaks centered at 465, 450, 434, 368, 399, and 314 nm, which correspond to transitions from the ground state $^6A_1(S)$ of tetrahedral Mn(II) to the excited states of $^4T_1(^4G)$, $^4T_2(^4G)$, $^4A_1(^4G)$, $^4E(^4G)$, $^4T_2(^4D)$, $^4E(^4D)$, and $^4T_1(^4P)$, respectively. For **4**, the indicated transition peaks appear at 466, 448, 400, 370, and 341 nm. The band gaps of **3** and **4** were obtained using Kubelka-Munk model for band gap determination (Figure 20). Direct conversion of the absorbance peaks into electron volts would result in overestimation of the band gap, since the peak centers represent the most frequent transitions, but not necessarily the band gap.

To determine the band gap, the K-M function of diffraction reflectance was converted into $[F(R)\bullet eV]^2$ and plotted versus eV. The extrapolation of the straight part of every peak leads to a certain x-axis intercept, which corresponds to the lowest energy for particular electronic transition.[24] For **3**, such transitions are at 2.38, 2.50, 2.75, 3.15, and 3.45 eV. Thus, the band gap for **3** is 2.38 eV. Similar calculations for **4** result in 2.38, 2.75, 3.15, and 3.45 eV, and the band gap is the lowest energy transition, which is 2.38 eV. Transitions above 4.0 eV are considered high energy bands, which are irrelevant to this study. The PL emission for both **3** and **4** is at 2.38 eV with width at half maximum of 40 nm, which implies the dependence of the emission wavelength not on the organic cation, but on the tetrahedral Mn center only. Therefore, interchanging different organic cations with relatively similar size would not alter the photoluminescent properties of the Mn center. This idea can be developed further by modifying the physical properties of photoluminescent compound, such as thermal stability and wettability, while having the same photoluminescent properties. Both ground products, **3** and **4**, exhibit PL-QY of 47%.

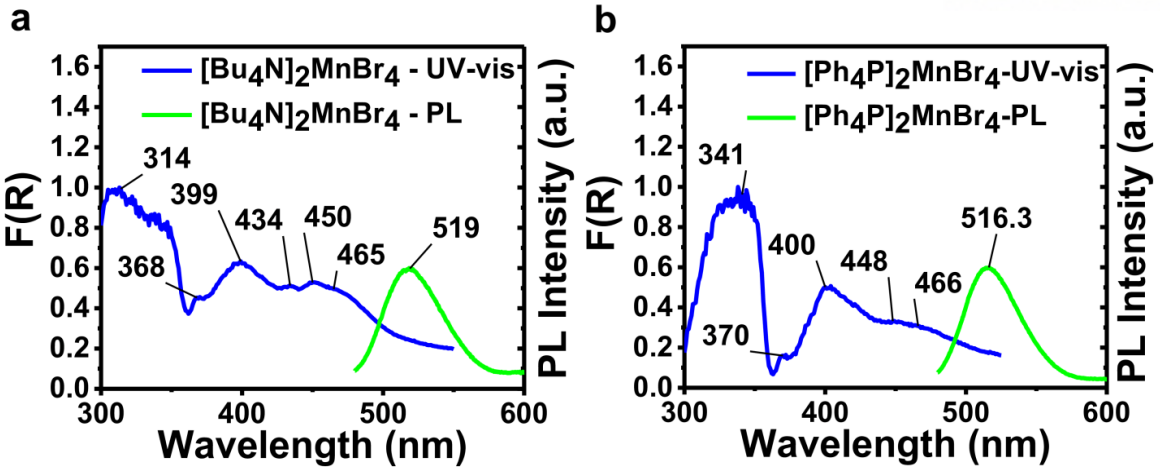

Figure 19. Solid-state diffusion reflectance and PL versus wavelength plots for (a) **3** and (b) **4** excited at 380 nm.

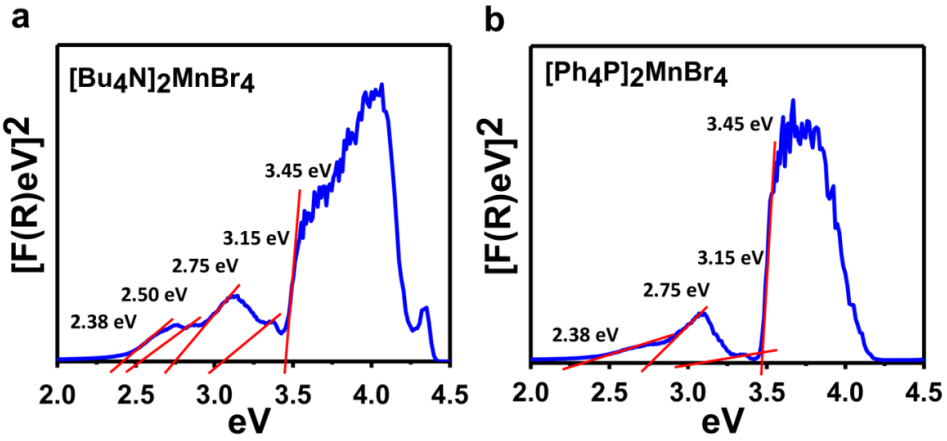

Figure 20. $[F(R)\bullet eV]^2$ vs. eV plot for determination of band gap of (a) **3** and (b) **4**.

To further investigate optical properties, we performed a low photon energy absorption analyses on **3** and **4** by measuring the fluorescent emission from the samples while exciting with low energy laser beams. The low energy photon absorption can happen when several photons with lower energy than the band gap of a material are absorbed simultaneously in order to excite an electron from the ground to excited state. The band gaps of **3** and **4** are 2.38 eV, with an absorption onset at around 516 nm. To observe the low energy photon absorption, the compounds were excited in the range between 640-820 nm with increments of 20 nm. When excited at 640-700 nm, both **3** and **4** show similar emission pattern, with peaks at 554, 573, 597, 605, and 609 nm (Figure 21a,c). These emissions are below the band gap of the material, and they are resulted from relaxation of trapped excited states. Since the energy provided for excitation is insufficient to do the full transition, an exciton is trapped in the crystalline structure of the compounds with the energy between HOMO and LUMO, and releases its energy by consecutive photon emission. However, when exciting with energy

below 700 nm down to 820 nm, the materials exhibit a distinctive emission peak at 450 nm that shifts toward higher wavelength as the excitation wavelength increases (Figure 21b, d). The emission peaks appear between 440 and 550 nm, intensities of which are several magnitudes lower compared to the one-photon absorption-emission. This range corresponds to the emission range of one-photon process, where the emission peak appears centered at 520 nm with the width at half maximum of 40 nm. The excitation energies used in these measurements are between 1.51 eV and 1.72 eV for each photon, which facilitated the lowest energy electron transitions in tetrahedral Mn(II) metal center, that are from $^6A_1(S)$ to $^4T_1(^4G)$, $^4T_2(^4G)$, $^4A_1(^4G)$, $^4E(^4G)$, $^4T_2(^4D)$, $^4E(^4D)$, and $^4T_1(^4P)$.

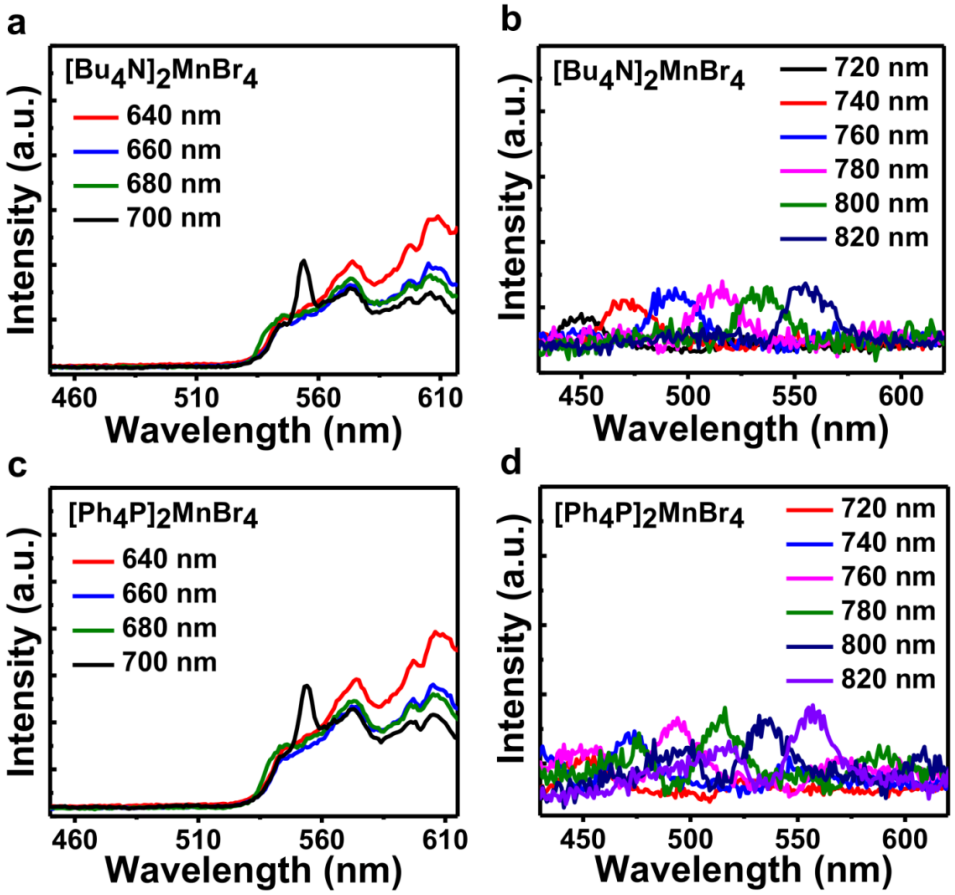

Figure 21. (a-b) PL spectra of **3** excited between 640 and 820 nm, and (c-d) PL spectra of **4** excited between 640 and 820 nm.

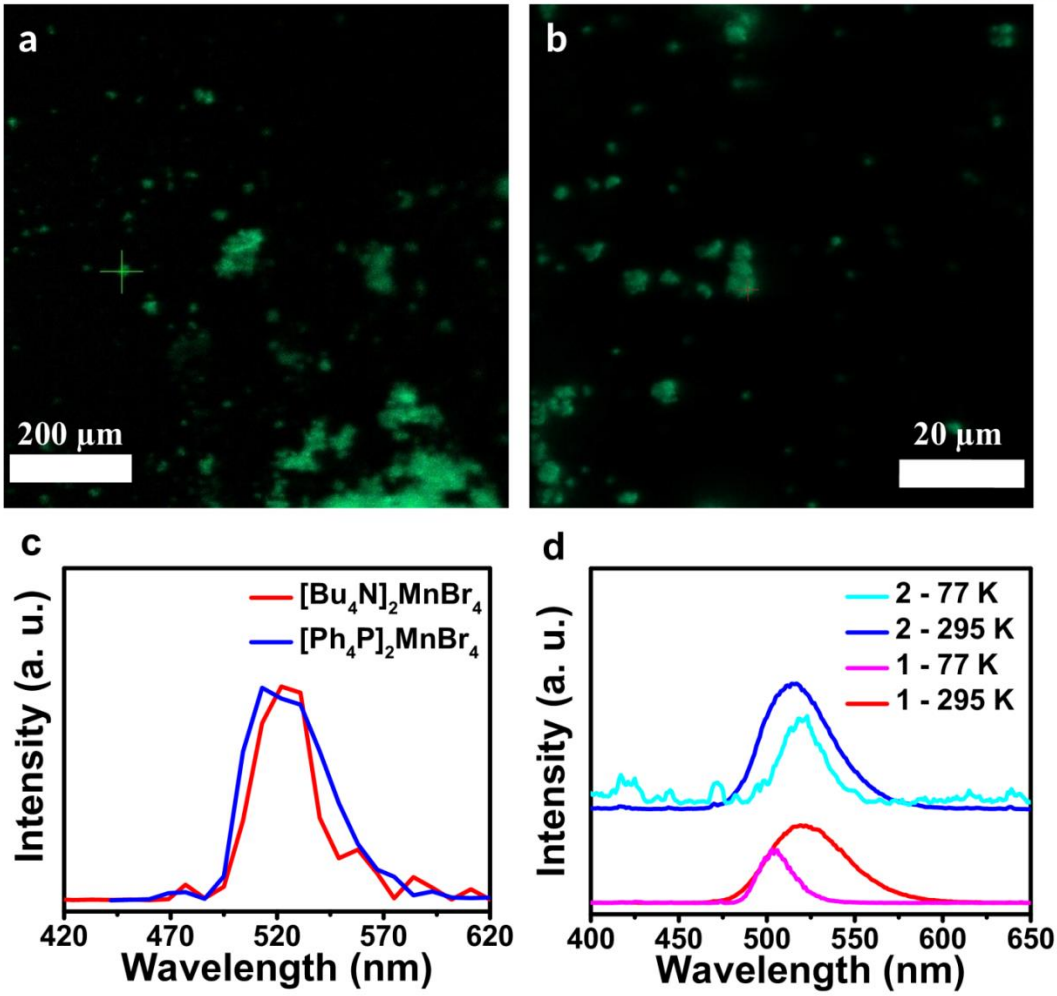

Figure 22. Confocal microscopy images of (a) **3** and (b) **4** excited with 488 nm laser source; (c) Single point PL emission graphs of **3** and **4** collected from regions indicated with cross marks in (a-b); Bulk PL emissions of **3** and **4** collected under room temperature and at 77 K.

Single crystal images in the figures 22a-b obtained from confocal laser scanning microscopy indicate that each crystal possesses bright green PL at 520 nm upon irradiating with 405 nm laser beam. The normalized single-point emissions from both compounds are shown in the figure 22c. The emission peak position of single particle is same as powder sample, ruling out the shape dependent PL emission. To check the emission behavior with temperature, we have taken emission spectra at 295 and 77K (Figure 22d). Both compounds exhibit blue shifted PL wavelength at 77K as compared to 295K and those PL peaks are reversibly interchanged with temperature. The blue shifts for **3** and **4** are 15 nm (520 to 505 nm) and 5 nm (520 nm to 515 nm), respectively. Thus, **4** will be better for temperature sensitive solid state lighting device applications.

3.2.3. Computational analysis

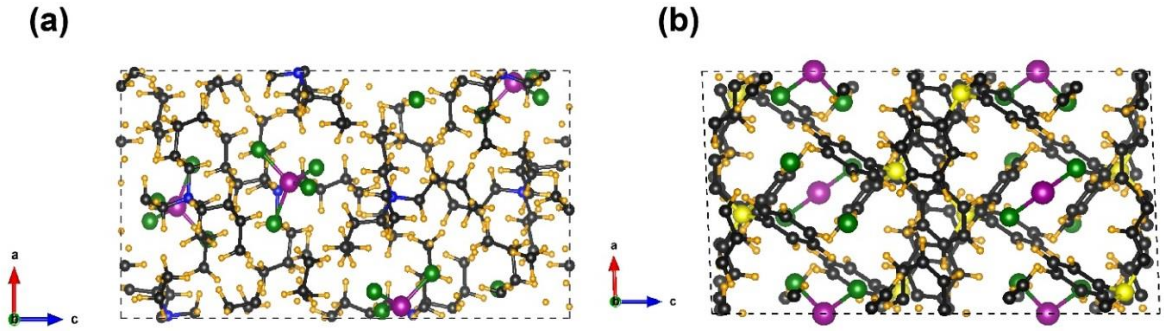

Figure 23. Crystal structure for (a) $[Bu_4N]_2[MnBr_4]$ and (b) $[Ph_4P]_2[MnBr_4]$. (H = orange, C = black, N = blue, Mn = pink, Br = green, P = yellow).

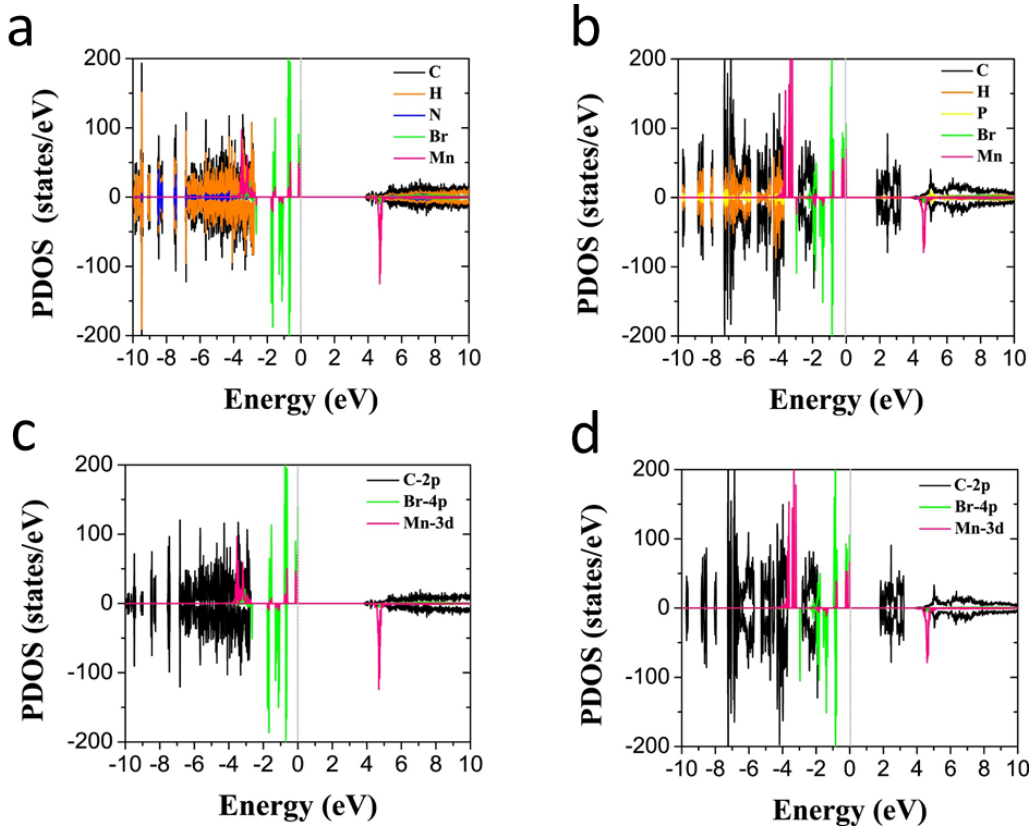

Figure 24. Projected density of states for (a) **3** and (b) **4** per element in the unit cell, and partial orbits of C, Br, and Mn for (c) **3** and (d) **4**. Fermi level is at zero and is indicated by short dashed vertical line.

To better understand the electronic structure of **3** and **4**, we have calculated the projected density of states (PDOS) and decomposed charge density. The relaxed structures are shown in Figure 23. Figure 24 shows the calculated PDOS for **3** and **4**. At the band edges, it is evident from PDOS for **3** that the orbital contribution to valence band stems primarily from Br 4*p* and Mn 3*d* states, while

contribution to conduction band is from C 2*p* and Mn 3*d* states. For the case of **4** the contribution to valence band edges is dominated from Br 4*p* and Mn 3*d* states and the conduction band is dominated by C 2*p* states. For both compounds, several empty bands with higher energy than conduction band edge are formed by C 2*p* orbitals. Br 4*s* and Mn 4*s* orbitals show no contributions to both conduction and valence bands in both compounds. N 2*p* and P 3*p* orbitals contribute to valence band in **3** and **4**, respectively, but these states are far away from band edges. The calculated band gaps of **3** and **4** are 1.9 eV and 3.34 eV, respectively.

Further, we have also examined the charge density associated with valence band maximum (VBM) and conduction band minimum (CBM) for **3** and **4**. Decomposed charge densities are plotted in Figure 4 for **3** and **4**. From figure 25, one notes for **3** that VBM is derived from the Br 4*p* and Mn 3*d* states interactions, while CBM is derived from C 2*p*. Similarly, for **4**, the contribution to VBM comes from the Br 4*p* and Mn 3*d* interaction, while CBM is derived from C 2*p* interaction.

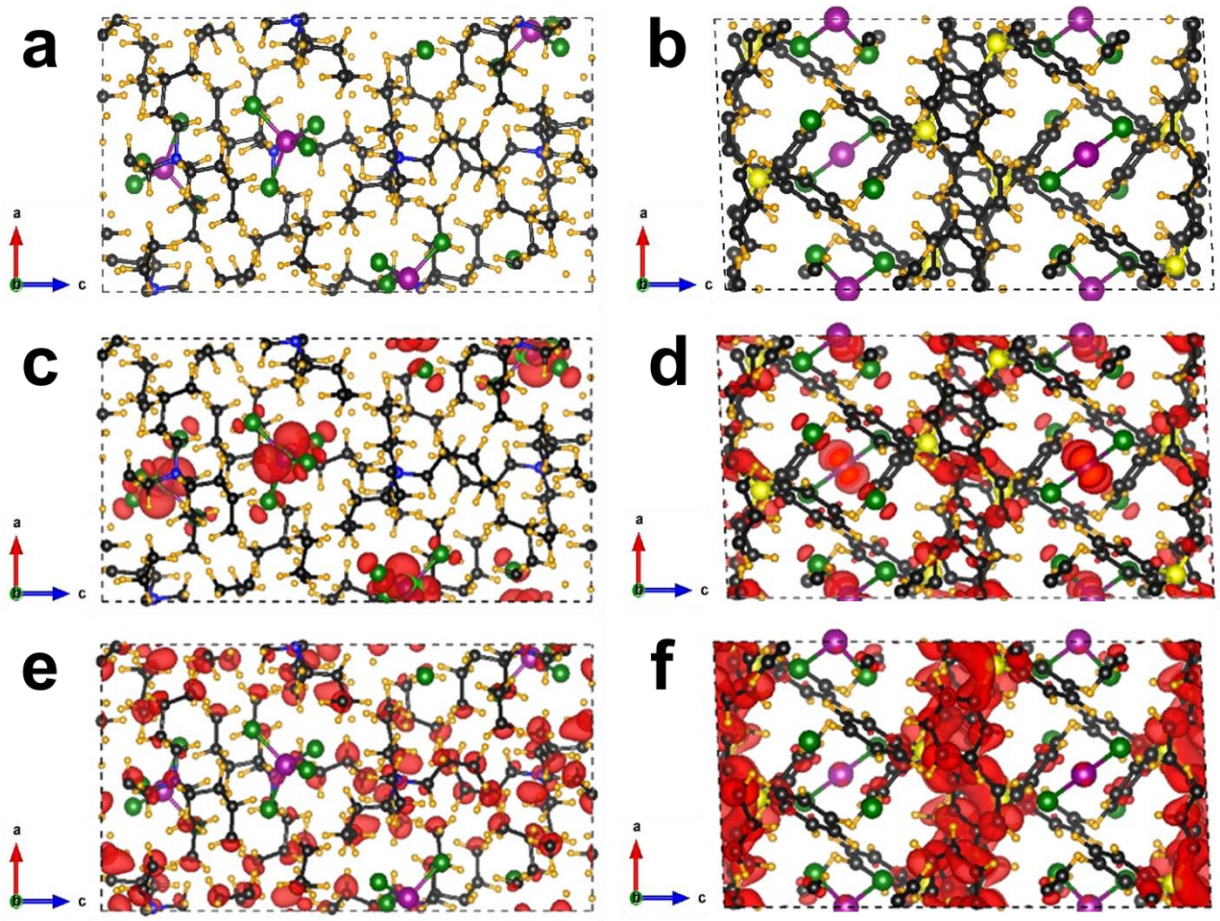

Figure 25. Crystal structure for (a) **3** and (b) **4**; Charge density corresponding to states near VBM for (c) **3** and (d) **4**, and near CBM for (e) **3** and (f) **4**. Iso-surface value is $5x10^{-3}$ eV/Å^3. (H: orange, C: black, N: blue, Mn: pink, Br: green, P: yellow).

IV. CONCLUSION

In conclusion, solid-state mechanochemical syntheses approach was utilized in order to prepare range of low-dimensional lead-free fluorescent organic-inorganic hybrid compounds. The mechanochemical synthesis protocol can be accomplished in under 10 minutes with 100% yield of the final product. Moreover, the technique allows free control and manipulation over the composition of the hybrids, and can be easily modified to obtain compounds with different ration of constituents. Mainly, 0D-$[Me_4N]_2MnCl_4$, 0D-$[Bu_4N]_2MnBr_4$, 0D-$[Bu_4N]_2MnBr_4$, and 1D-$[Me_4N]MnCl_3$, and other derivatives of a similar structure were synthesized via solvent-free solid-state mechanochemical grinding of precursor salts in mortar. The obtained hybrids were subjected to physical and photochemical analysis to get insight into their photophysical properties. The hybrids showed exact match upon comparing mechanochemically synthesized PXRD and solution-processed single crystal XRD profiles. Compounds **1-4** had excellent thermal stability, with **4** having the highest stability at 400˚C and reversible melting/crystallization dynamics. The **1**, **3**, **4** showed PL emission in green region at 520 nm, while **2** exhibited PL emission in red region at 620 nm. Such difference in PL nature of **2** was achieved by simply changing the ratio of organic to inorganic precursors from 2:1 to 1:1, which altered the coordination environment of metal center, and ultimately converting a 0D hybrid into linear 1D hybrid. The obtained hybrids **3** and **4** exhibit emission phenomena upon exciting with above and below band gap photons. Such phenomenon was never explored as yet, and was observed in our hybrids using simple PL techniques. While lead-containing organic-inorganic perovskites are in great demand, the toxicity of lead hampers their practical applications. In this context, our as-synthesized products, which are environmentally-friendly and easy-to-synthesize, can replace toxic materials in future optoelectronic device applications. Moreover, the scope of the methodology of mechanochemical synthesis of low-dimensional photoluminescent compounds can be easily extended into synthesis of other low-dimensional compounds, which can greatly reduce the synthesis time, as well as efforts in the production of delicate devices for solid-state optoelectronic applications.

Finally, I would like to mention that this work was done by the help of Dr. Atanu Jana, Qiankai Ba, and Arun S. Nissimagoudar, under the supervision of Prof. Kwang S. Kim, and this manuscript is to be submitted to an international scientific journal. The title of the publication is subject to change.[25]

REFERENCES

[1] a) N.-G. Park, M. Grätzel, T. Miyasaka, K. Zhu, K. Emery, *Nature Energy* **2016**, *1*, 16152; b) W. S. Yang, B.-W. Park, E. H. Jung, N. J. Jeon, Y. C. Kim, D. U. Lee, S. S. Shin, J. Seo, E. K. Kim, J. H. Noh, S. I. Seok, *Science* **2017**, *356*, 1376-1379; c) C. W. Myung, J. Yun, G. Lee, K. S. Kim, *Advanced Energy Materials* **2018**, *8*, 1702898.

[2] K. Wang, G. Li, S. Wang, S. Liu, W. Sun, C. Huang, Y. Wang, Q. Song, S. Xiao, *Advanced Matererials* **2018**, *30*, 1801481.

[3] T. Chiba, Y. Hayashi, H. Ebe, K. Hoshi, J. Sato, S. Sato, Y.-J. Pu, S. Ohisa, J. Kido, *Nature Photonics* **2018**, *12*, 681-687.

[4] P. J. Cegielski, A. L. Giesecke, S. Neutzner, C. Porschatis, M. Gandini, D. Schall, C. A. R. Perini, J. Bolten, S. Suckow, S. Kataria, B. Chmielak, T. Wahlbrink, A. Petrozza, M. C. Lemme, *Nano Lett.* **2018**, *18*, 6915-6923.

[5] N. R. E. Laboratory, **2018**.

[6] a) M. I. Saidaminov, O. F. Mohammed, O. M. Bakr, *ACS Energy Letters* **2017**, *2*, 889-896; b) H. Lin, C. Zhou, Y. Tian, T. Siegrist, B. Ma, *ACS Energy Letters* **2018**, *3*, 54-62.

[7] P. Billen, E. Leccisi, S. Dastidar, S. Li, L. Lobaton, S. Spatari, A. T. Fafarman, V. M. Fthenakis, J. B. Baxter, *Energy* **2019**, *166*, 1089-1096.

[8] J. I. Zink, G. E. Hardy, G. Gliemann, *Inorg. Chem.* **1980**, *19*, 488-492.

[9] F. A. Cotton, D. M. Goodgame, M. Goodgame, *J. Am. Chem. Soc.* **1962**, *84*, 167-172.

[10] J. Chen, Q. Zhang, F.-K. Zheng, Z.-F. Liu, S.-H. Wang, A. Q. Wu, G.-C. Guo, *Dalton Transactions* **2015**, *44*, 3289-3294.

[11] M. Bortoluzzi, J. Castro, F. Enrichi, A. Vomiero, M. Busato, W. Huang, *Inorg. Chem. Commun.* **2018**, *92*, 145-150.

[12] Y. Zhang, J. Liu, Z. Wang, Y. Xue, Q. Ou, L. Polavarapu, J. Zheng, X. Qi, Q. Bao, *Chem. Commun.* **2016**, *52*, 13637-13655.

[13] a) Q. A. Akkerman, S. G. Motti, A. R. Srimath Kandada, E. Mosconi, V. D'Innocenzo, G. Bertoni, S. Marras, B. A. Kamino, L. Miranda, F. De Angelis, A. Petrozza, M. Prato, L. Manna, *J. Am. Chem. Soc.* **2016**, *138*, 1010-1016; b) X. Gong, O. Voznyy, A. Jain, W. Liu, R. Sabatini, Z. Piontkowski, G. Walters, G. Bappi, S. Nokhrin, O. Bushuyev, M. Yuan, R. Comin, D. McCamant, S. O. Kelley, E. H. Sargent, *Nature Materials* **2018**, *17*, 550-556; c) M. D. Smith, B. A. Connor, H. I. Karunadasa, *Chem. Rev.* **2019**, *119*, 3104-3139; d) M.-H. Tremblay, F. Thouin, J. Leisen, J. Bacsa, A. R. Srimath Kandada, J. M. Hoffman, M. G. Kanatzidis, A. D. Mohite, C. Silva, S. Barlow, S. R. Marder, *J. Am. Chem. Soc.* **2019**, *141*, 4521-4525.

[14] a) A. Jana, M. Mittal, A. Singla, S. Sapra, *Chem. Commun.* **2017**, *53*, 3046-3049; b) P. Pal, S. Saha, A. Banik, A. Sarkar, K. Biswas, *Chemistry – A European Journal* **2018**, *24*, 1811-1815; c) Z.-Y. Zhu, Q.-Q. Yang, L.-F. Gao, L. Zhang, A.-Y. Shi, C.-L. Sun, Q. Wang, H.-L. Zhang, *The Journal of Physical Chemistry Letters* **2017**, *8*, 1610-1614.

[15] C. Zhou, Y. Tian, M. Wang, A. Rose, T. Besara, N. K. Doyle, Z. Yuan, J. C. Wang, R. Clark, Y. Hu, T. Siegrist, S. Lin, B. Ma, *Angew. Chem. Int. Ed.* **2017**, *56*, 9018-9022.

[16] Y.-L. Wei, J. Jing, C. Shi, H.-Y. Ye, Z.-X. Wang, Y. Zhang, *Inorganic Chemistry Frontiers* **2018**, *5*, 2615-2619.

[17] a) G. Kresse, J. Furthmüller, *Computational Materials Science* **1996**, *6*, 15-50; b) G. Kresse, J. Furthmüller, *Physical Review B* **1996**, *54*, 11169-11186.

[18] J. P. Perdew, K. Burke, M. Ernzerhof, *Phys. Rev. Lett.* **1996**, *77*, 3865-3868.

[19] Y. Qi, J. Wang, J. Shan, *International Journal of Systems Science* **2018**, *49*, 662-676.

[20] A. Tkatchenko, M. Scheffler, *Phys. Rev. Lett.* **2009**, *102*, 073005.

[21] T. A. Mellan, F. Corà, R. Grau-Crespo, S. Ismail-Beigi, *Physical Review B* **2015**, *92*, 085151.

[22] a) J. A. Barreda-Argüeso, L. Nataf, Y. Rodríguez-Lazcano, F. Aguado, J. González, R. Valiente, F. Rodríguez, H. Wilhelm, A. P. Jephcoat, *Inorg. Chem.* **2014**, *53*, 10708-10715; b) S.

Tancharakorn, F. P. A. Fabbiani, D. R. Allan, K. V. Kamenev, N. Robertson, *J. Am. Chem. Soc.* **2006**, *128*, 9205-9210.

[23] R. A. Davoglio, G. Cabello, J. F. Marco, S. R. Biaggio, *Electrochim. Acta* **2018**, *261*, 428-435.

[24] G. Kortüm, W. Braun, G. Herzog, *Angewandte Chemie International Edition in English* **1963**, *2*, 333-341.

[25] A. Jana, S. Zhumagali, Q. Ba, A. S. Nissimagoudar, K. S. Kim, **2019**.

Acknowledgements

I am immensely thankful to UNIST for providing a scholarship during my Master's Degree studies.

Prof. Kwang S. Kim has given me this opportunity to do my Master's Thesis research under his supervision, for which I am grateful.

Dr. Atanu Jana has been an ideal mentor and a guide, offering advice and encouragement throughout this work. I'm proud of, and grateful for, my time working with Dr. Jana.

Prof. Wonyoung Choe and Prof. Hoi Ri Moon taught a great deal about research nuances during their classes, which helped me a lot throughout my work.

Qiankai Ba provided any help when needed, and it was a pleasure to share a workspace with him.

Many thanks to my parents, friends, and colleagues.

Eternal gratitude to Aika for her patience and support through these years.